

1 **Antibody-dependent enhancement (ADE) of SARS-CoV-2 infection**
2 **in recovered COVID-19 patients: studies based on cellular and**
3 **structural biology analysis**

4
5 Fan Wu^{1*#}, Renhong Yan^{2,3#}, Mei Liu^{1#}, Zezhong Liu^{1#}, Yingdan Wang^{1#}, Die Luan¹,
6 Kaiyue Wu¹, Zhigang Song¹, Tingting Sun¹, Yunping Ma¹, Yuanyuan Zhang^{2,3}, Qimin
7 Wang¹, Xiang Li¹, Ping Ji¹, Yaning Li⁴, Cheng Li¹, Yanling Wu¹, Tianlei Ying¹, Yumei
8 Wen¹, Shibo Jiang¹, Tongyu Zhu^{1*}, Lu Lu^{1*}, Yongzhen Zhang^{1*}, Qiang Zhou^{2,3*}, Jinghe
9 Huang^{1*}

10
11 ¹ Shanghai Public Health Clinical Center and Key Laboratory of Medical Molecular Virology
12 (MOE/NHC/CAMS), School of Basic Medical Sciences, Fudan University, Shanghai, China.

13 ² Center for Infectious Disease Research, Zhejiang Provincial Laboratory of Life Sciences and
14 Biomedicine, Key Laboratory of Structural Biology of Zhejiang Province, School of Life Sciences,
15 Westlake University, 18 Shilongshan Road, Hangzhou 310024, Zhejiang Province, China.

16 ³Institute of Biology, Westlake Institute for Advanced Study, 18 Shilongshan Road, Hangzhou
17 310024, Zhejiang Province, China.

18 ⁴Beijing Advanced Innovation Center for Structural Biology, Tsinghua-Peking Joint Center for Life
19 Sciences, School of Life Sciences, Tsinghua University, Beijing 100084, China.

20
21 #These authors contributed equally.

22 *Correspondence to: Dr. Jinghe Huang, 86-21-37990333-7326, Email:
23 Jinghehuang@fudan.edu.cn; Dr. Fan Wu, 86-21-37990333-5295, Email:
24 wufan@fudan.edu.cn; Dr. Qiang Zhou, 86-0571-87969653, Email:
25 zhouqiang@westlake.edu.cn; Dr. Yongzheng Zhang, 86-21-37990333, Email:
26 zhangyongzhen@shphc.org.cn; Dr. Lu Lu, 86-21-54237671, Email: lul@fudan.edu.cn;
27 or Dr. Tongyu Zhu, 86-21-37990333, Email: zhutongyu@shphc.org.cn.

28
29 **Keywords:** COVID-19; SARS-CoV-2; ADE; Neutralizing antibody

30
31

NOTE: This preprint reports new research that has not been certified by peer review and should not be used to guide clinical practice.

32 **Abstract**

33 Antibody-dependent enhancement (ADE) has been reported in several virus infections
34 including dengue fever virus, severe acute respiratory syndrome (SARS) and Middle
35 East respiratory syndrome (MERS) coronavirus infection. To study whether ADE is
36 involved in COVID-19 infections, *in vitro* pseudotyped SARS-CoV-2 entry into Raji
37 cells, K562 cells, and primary B cells mediated by plasma from recovered COVID-19
38 patients were employed as models. The enhancement of SARS-CoV-2 entry into cells
39 was more commonly detected in plasma from severely-affected elderly patients with
40 high titers of SARS-CoV-2 spike protein-specific antibodies. Cellular entry was
41 mediated via the engagement of FcγRII receptor through virus-cell membrane fusion,
42 but not by endocytosis. Peptide array scanning analyses showed that antibodies which
43 promote SARS-CoV-2 infection targeted the variable regions of the RBD domain. To
44 further characterize the association between the spike-specific antibody and ADE, an
45 RBD-specific monoclonal antibody (7F3) was isolated from a recovered patient, which
46 potently inhibited SARS-Cov-2 infection of ACE-2 expressing cells and also mediated
47 ADE in Raji cells. Site-directed mutagenesis the spike RBD domain reduced the
48 neutralization activity of 7F3, but did not abolish its binding to the RBD domain.
49 Structural analysis using cryo-electron microscopy (Cryo-EM) revealed that 7F3 binds
50 to spike proteins at a shift-angled pattern with one “up” and two “down” RBDs,
51 resulting in partial overlapping with the receptor binding motif (RBM), while a
52 neutralizing monoclonal antibody that lacked ADE activity binds to spike proteins with
53 three “up” RBDs, resulting in complete overlapping with RBM. Our results revealed
54 that ADE mediated by SARS-CoV-2 spike-specific antibodies could result from
55 binding to the receptor in slightly different pattern from antibodies mediating
56 neutralizations. Studies on ADE using antibodies from recovered patients via cell
57 biology and structural biology technology could be of use for developing novel
58 therapeutic and preventive measures for control of COVID-19 infection.
59

60 **Introduction**

61 The global pandemic of coronavirus disease 2019 (COVID-19), caused by severe acute
62 respiratory syndrome coronavirus 2 (SARS-CoV-2), had resulted in a total of 34.8
63 million cases of infection and over 1 million deaths worldwide by October 4, 2020,¹.
64 No therapeutic drugs against SARS-CoV-2 are currently available, and the development
65 of vaccines is considered as the most effective approach to control the ongoing
66 pandemic. Multiple platforms are being developed as a SARS-CoV-2 vaccine,
67 including DNA- and RNA-based formulations, recombinant viral subunits, replicating
68 viral vectors and purified inactivated viral particles, are under development, and several
69 vaccine candidates are presently being evaluated for efficacy in phase III trials².
70 Most vaccines incorporate SARS-CoV-2 spike (S) protein or its receptor-binding
71 domain (RBD) as immunogens. As the primary targets for neutralizing antibodies
72 (NAbs), the S protein and RBD are promising immunogens to induce protective NAbs
73 in vaccine recipients³⁻⁶. However, preclinical experience with severe acute respiratory
74 syndrome (SARS) and Middle East respiratory syndrome (MERS) vaccine candidates
75 has raised safety concerns about the potential for antibody-dependent enhancement
76 (ADE) induced by coronavirus S protein⁷⁻¹¹. ADE is an enhancement of viral entry into
77 immune cells mediated by antibody via the engagement of the Fc receptors^{12,13}. This
78 phenomenon has been documented with mosquito-borne flavivirus infections, such as
79 dengue¹⁴ and Zika viruses¹⁵. For dengue virus, the ADE of virus infection of immune
80 cells resulted in the enhancement of disease severity especially at the second infections
81 with different virus strains in humans¹⁶. For coronaviruses, ADE has been mainly
82 reported in animal models infected by SARS-CoV, MERS-CoV and feline coronavirus,
83 in which exacerbated lung disease was observed when vaccinated animals were infected
84 with viruses^{7,10,17}. In both SARS-CoV and MERS-CoV infections, ADE was mediated
85 with antibodies against spike (S) proteins^{7,9}. Although S protein-specific antibodies
86 were elicited in most patients with COVID-19, the antibody titers were higher in elderly
87 patients of COVID-19, and stronger antibody response was associated with delayed
88 viral clearance and increased disease severity in patients^{18,19}. Hence it is reasonable to

89 speculate that S protein-specific antibodies may contribute to disease severity during
90 SARS-CoV-2 infection^{11,20,21}. Furthermore, the potential for such ADE responses is of
91 concern for SARS-CoV-2 in the use of convalescent plasma or antibodies as a treatment
92 in COVID-19 patients^{22,23}. However, whether SARS-CoV-2 specific antibodies or
93 convalescent plasma could promote virus infection of immune cells or enhance disease
94 severity has not been documented.

95 Here, we used an *in vitro* pseudotyped SARS-CoV-2 infection assay to evaluate the
96 ability of plasma and antibodies from recovered COVID-19 patients to promote SARS-
97 CoV-2 infection of immune cells, and analyzed the associated clinical and
98 immunological characteristics.

99

100 **Results**

101 **Clinical Characteristics**

102 This study enrolled 222 patients in total who had recovered from COVID-19 and were
103 discharged from the Shanghai Public Health Clinical Center as of April 23, 2020. Of
104 the 222 patients, 205 had mild symptoms and 17 had severe symptoms. The median
105 [interquartile range, IQR] age of patients was 53 [38-65] years; 49 % of the patients
106 were female. The median length of hospital stay was 17 [13-24] days, and the median
107 disease duration was 23 [18-30] days.

108

109 **Plasma from recovered patients of COVID-19 showed enhancement of SARS- 110 CoV-2 infection of immune cells**

111 We collected plasma samples from 205 patients who had recovered from mild COVID-
112 19 at the time of discharge (median days 22), as well as 17 patients who had recovered
113 from severe COVID-19 at the time before discharge (median days 34), and evaluated
114 the enhancement of pseudotyped SARS-CoV-2 infection *in vitro* for each patient
115 plasma by using Raji cells that are lymphoma cells derived from human B lymphocytes.
116 The cells expressed human Fc γ RII (CD32) and were used for ADE assay of SARS-CoV

117 previously²⁴. Plasma from 16 (8%) of the recovered patients with mild COVID-19 and
118 13 (76%) of the recovered patients with severe COVID-19 (N=17, median age 66)
119 showed a concentration-dependent enhancement of SARS-CoV-2 infection of Raji cells,
120 indicated by the increase of luciferase expression in Raji cells (Figure S1,1A). The
121 enhancement of virus infection was significantly higher in plasma from COVID-19
122 patients compared with plasma from uninfected controls ($P < 0.0001$, Figure 1B, S1).
123 Moreover, plasma from these 29 patients also showed detectable enhanced infection of
124 Raji cells of pseudotyped bat-origin SARS-like coronavirus, either RS3367 or WIV1
125 ($P = 0.0108$ or $P = 0.0046$, Figure 1B), while none of the plasma showed enhancement
126 of SARS-CoV infection (Figure 1B).

127 The enhancement of SARS-CoV-2 infection by patient plasma was also observed when
128 K562 cells derived from human monocytes were used as targets ($P = 0.0006$, Figure S2,
129 1C). Furthermore, the enhancement of SARS-CoV-2 infection was also confirmed
130 when cultured primary B cells were used as targets. As shown in Figure S3, eight
131 representative positive plasma samples, four from patients with mild COVID-19 and
132 the other four from patients with severe COVID-19, showed concentration-dependent
133 enhancement of SARS-CoV-2 infection of primary B cells. These eight plasma
134 mediated significantly higher SARS-CoV-2 infection than control plasma from
135 uninfected donors ($P = 0.004$, Figure 1D).

136 In the following studies, Raji cells were used as targets on the mechanism of
137 enhancement of SARS-CoV2 infection because they were easily maintained and
138 generated higher luciferase reading than K562 cells and primary B cells.

139

140 **Enhancement of SARS-CoV-2 infection was mediated by IgG antibodies** 141 **engagement of FcγRII receptor**

142 To confirm whether the enhancement of SARS-CoV-2 infection was mediated by
143 antibodies, we purified IgG from the plasma and measured the enhancement of SARS-
144 CoV-2 infection of Raji cells by purified antibodies and IgG-depleted plasma,

145 respectively. As shown in Figure 1E, purified IgG showed enhancement of SARS-CoV-
146 2 infection, which was similar to plasma from patients. The depletion of IgG from
147 plasma completely abolished the infection of Raji cells, confirming that the
148 enhancement of SARS-CoV-2 infection was mediated by IgG in plasma. We further
149 used anti-CD32 antibody to block the cell surface Fc γ RII receptor to evaluate the
150 engagement of Fc γ RII receptor in promoting SARS-CoV-2 infection. The addition of
151 anti-CD32 antibody eliminated the enhancement of SARS-CoV-2 infection by both
152 plasma (Figure 1F) and purified IgG (Figure 1G) from patients. These results indicated
153 that the *in vitro* enhancement of SARS-CoV-2 infection by patient plasma was mediated
154 by IgG antibodies with the engagement of Fc γ RII receptor, which is similar to the ADE
155 of virus infections including SARS-CoV, MERS-CoV, Zika, and dengue viruses.

156

157 **ADE is more likely to develop in elderly patients with severe and critical condition,**
158 **longer hospital stays and disease duration**

159 We investigated the clinical characteristics of 29 recovered patients whose plasma
160 showed ADE effect. The median age of these patients (65 [58-72] years) was
161 significantly higher than the patients without ADE effect (50 [37-64] years, $P < 0.0001$,
162 Figure 1H). The median disease duration time and the length of hospital stays of
163 patients whose plasma showed ADE was significantly longer than patients without
164 ADE effect (35 [23-60] days *vs.* 22 [18-29] days, $P < 0.0001$, and 30 [19-55] days *vs.*
165 17 [13-23] days, $P < 0.0001$, Figure 1I and 1J). These results indicated that ADE is more
166 likely to develop in elderly patients with severe and critical condition, longer hospital
167 stays and disease duration, suggesting a possible association of ADE with disease
168 severity in COVID-19 patients.

169 To evaluate whether the ADE effect resulted from pre-exposure to other pathogens in
170 elderly patients, we collected plasma from 18 uninfected elderly donors aged 60 to 80
171 years and tested them for ADE. None of the plasma from uninfected control donors
172 showed an ADE effect ($P = 0.3085$, Figure S4), confirming that ADE appeared to be

173 the result of SARS-CoV-2 infection.

174

175 **ADE is more likely to develop in patients with high titers of SARS-CoV-2 RBD-**
176 **and S1-specific antibodies**

177 Next, we evaluated the relationship between ADE effect and SARS-CoV-2-specific
178 antibodies. Significantly higher titers of SARS-CoV-2 NAbs ($P < 0.0001$, Figure 2A),
179 as well as RBD-specific ($P < 0.0001$) and S1-specific binding antibodies ($P < 0.0001$)
180 (Figure 2B), were found in plasma with ADE effect compared to plasma without ADE
181 effect, while S2-specific antibodies showed no difference. Then we evaluated the
182 kinetics of ADE effect, binding antibodies, and NAbs during the course of disease in
183 six patients for whom sequential plasma samples were available. The kinetics of ADE
184 development was similar among all patients, starting to increase at day 10 post-disease
185 onset, reaching their peak at day 20, and remaining stable for at least 40-81 days (Figure
186 2C and Figure S5A). The kinetics of titers of antibodies binding to RBD and S1 (Figure
187 2D and Figure S5B) was similar to the kinetics of ADE (Figure 2C and Figure S5B red
188 line), while the kinetics of NAbs in these patients was different. The titers of NAbs in
189 the six patients increased on day 10 post-disease onset and reached a very high level
190 around day 20 (median ID₅₀ = 2877) (Figure 2E and Figure S3C blue line). However,
191 NAb titers dramatically dropped to low levels (median ID₅₀ = 545) after day 30 post-
192 disease onset. These results indicated that high levels of binding antibodies might
193 contribute to the ADE of SARS-CoV-2 infection.

194

195 **ADE was mediated by antibodies binding to SARS-CoV-2 spike RBD subunits**

196 To further determine the role of spike-specific antibodies in mediating ADE of SARS-
197 CoV-2 infection, we incubated SARS-CoV-2 RBD and S1 proteins with plasma to block
198 the protein-specific antibodies before measuring the ADE effect of plasma samples.
199 Pre-incubation with SARS-CoV-2 RBD protein at a concentration as low as 0.1 µg/ml
200 could completely block the ADE effect of plasma from the representative patient 8

201 (Figure 3A), and pre-incubation with S1 protein at the concentration of 1 µg/ml could
202 also block the ADE effect (Figure 3B). However, pre-incubation with SARS-CoV RBD
203 or S1 protein did not change the ADE activity in plasma (Figure 3C and 3D). The
204 inhibition of ADE effect by SARS-CoV-2 RBD protein was also observed in the plasma
205 from other patients. As shown in Figure 3E, pre-incubation of 10 µg/ml SARS-CoV-2
206 RBD significantly reduced ADE effect mediated by plasma from six tested patients (P
207 = 0.009). These results indicated that the ADE of SARS-CoV-2 infection was mediated
208 by antibodies targeting SARS-CoV-2 spike RBD subunits.

209

210 **ADE of SARS-CoV-2 infection occurred through the virus-cell membrane fusion**

211 It was suggested that the ADE of viral infection was mediated by phagocytosis of
212 immune complexes via FcγRII / CD32 receptor²⁵. However, the addition of chloroquine,
213 a phagocytosis inhibitor which could raise the pH of phagolysosomes and inhibit the
214 phagocytosis of mononuclear cells²⁶, did not inhibit the ADE by the plasma, even at the
215 highest concentration of 50 µM (Figure 4A). In contrast, EK1 peptide, which has been
216 demonstrated to inhibit virus-cell membranes fusion by binding to the HR1 domain and
217 thus inhibiting the formation of the six-helix bundle (6HB) of SARS-CoV-2 S2
218 protein²⁷, blocked ADE of SARS-CoV-2 infection in a dose-dependent manner (Figure
219 4B). The inhibition of ADE effect by EK1 peptide, but not chloroquine, was observed
220 for six tested plasma samples with ADE effect (P = 0.0064, Figure 4C). These results
221 indicated that ADE of SARS-CoV-2 infection was mediated through virus-to-cell
222 membrane fusion, not phagocytosis.

223 The ability of plasma to promote virus-to-cell membrane fusion was confirmed by an
224 *in vitro* syncytium formation assay, using HEK-293T cells expressing the SARS-CoV-
225 2 S protein as effector cells and Raji cells as target cells. No syncytium formation
226 occurred in the presence of control plasma (Figure 4D, left). However, large syncytium
227 was induced by plasma from representative patients 5, 7, and 8 in a dose-dependent
228 manner (Figure 4D, middle; Figure 4E). The syncytium formation induced by plasma

229 from COVID-19 patients was specifically inhibited by the addition of EK1 peptide, but
230 not chloroquine (Figure 4D, right; Figure 4E). These results again confirmed that ADE
231 of SARS-CoV-2 infection by plasma was mainly through cell-to-cell membrane fusion,
232 a pathway involved in the formation of the six-helix bundle (6HB) of SARS-CoV-2 S2
233 protein, which could be inhibited by EK1 peptide.

234

235 **RBD-specific human NAb 7F3 with ADE effect enhanced SARS-CoV-2 infection**
236 **and promoted virus entry into Raji cells through the virus-cell membrane fusion**

237 We further evaluated the characterization of antibodies with ADE effect by isolating
238 two monoclonal antibodies (mAbs) from recovered COVID-19 patient. These two
239 mAbs, termed as 7F3 and 4L12, were isolated by *in vitro* single B cell culture and
240 subsequent high-throughput micro-neutralization screening assay from the same
241 recovered COVID-19 patient. Both of the antibodies potently neutralized SARS-CoV-
242 2 pseudovirus infection of 293T cells expressing ACE2 protein with an IC₅₀ of 0.00684
243 µg/ml and 0.00452 µg/ml, respectively (Figure 5A). The two antibodies bound to
244 SARS-CoV-2 RBD and S1 proteins, but not S2, in the ELISA assay (Figure 5B).
245 Antibody 7F3 had higher binding affinity to RBD protein with a K_D value of $0.69 \pm$
246 0.03 nM, when compared to antibody 4L12 which bound to RBD with a K_D value of
247 1.49 ± 0.06 nM (Figure 5C). Antibody 7F3 showed a concentration-dependent
248 enhancement of SARS-CoV-2 infection of Raji cells (Figure 5D), while antibody 4L12
249 did not. The enhancement of SARS-CoV-2 infection by antibody 7F3 was also
250 dependent on the interaction between antibody Fc region with FcγRII receptor, because
251 the enhancement could be completely abolished by either removal of antibody Fc
252 region (Figure 5E) or blocking FcγRII receptor with anti-CD32 antibody (Figure 5F).
253 We also compared the ADE effect of different isotypes of 7F3 antibodies which were
254 generated by linking different heavy-chain constant regions to the same variable region
255 of 7F3 antibody. The IgG1 isotype showed the strongest ADE effect, IgG4 isotype
256 showed detectable ADE effect, while IgG2 and IgG3 did not show any detectable ADE

257 (Figure 5G), possibly resulting from the different binding affinity to Fc γ R2 receptor on
258 Raji cells. Consistent with the observations for plasma samples from recovered patients,
259 antibody 7F3-mediated enhancement of SARS-CoV-2 infection could be specifically
260 reduced by pre-incubation with RBD protein of SARS-CoV-2, but not from SARS-CoV
261 virus (Figure 5H), and the ADE could also be blocked by fusion-inhibitor EK1 peptide,
262 but not chloroquine (Figure 5I), suggesting that antibody 7F3-mediated ADE of SARS-
263 CoV-2 infection of Raji cells also occurred through virus-to-cell membrane fusion.

264

265 **Peptide scanning for hot spots in RBD associated with ADE effect**

266 Next, we explored the epitopes in RBD to which patient plasma and NAb 7F3 bound
267 and induced ADE. We synthesized a series of 20-mer peptides with 10 amino acid
268 overlap spanning the RBD region (304-593) to block the ADE of patient plasma and
269 antibody 7F3. Peptides from the S1 region, i.e., 304-323, 364-383, 544-563, 564-583,
270 and 574-593, dramatically blocked the ADE of both patient plasma (Figure 6A) and
271 7F3 (Figure 6B) and decreased >70 % of AUC (Figure 6C). Peptides from S1 regions
272 454-473 and 484-503 decreased 50-62% of the AUC for both ADE patient plasma and
273 7F3. Peptides from S1 regions 484-403 and 525-543 specifically blocked ADE patient
274 plasma, but not 7F3. These results suggested that several epitopes in RBD were
275 associated with ADE by antibodies.

276

277 **ADE antibody 7F3 and non-ADE antibody 4L12 shared overlapping epitopes but** 278 **showed different binding abilities to RBD**

279 To more precisely map the epitopes on RBD recognized by antibody 7F3, we
280 introduced single amino acid substitutions into the spike RBD domain and constructed
281 25 spike mutants, including seven mutants that were reported to be resistant to NAbs²⁸,
282 as well as a prevalent mutant D614G²⁹ (Figure 7, highlighted in blue), and evaluated
283 their sensitivity to neutralization of antibody 7F3. As shown in Figure 7A, 7F3
284 neutralized all seven mutants that resistant to NAbs and the prevalent mutant D614D.
285 Three amino acid substitutions, including F342L, P491A, and E516A exhibited

286 complete resistance to the neutralization of both 7F3 and 4L12 (IC₅₀ >50 µg/ml),
287 suggesting overlapping between the epitopes of 7F3 and 4L12.

288 We expressed the RBD protein mutants and measured the binding ability of 7F3 to these
289 mutants relative to wild type RBD. None of these mutations except P491A affected 7F3
290 and 4L12 binding to spike protein (Figure 7B and 7C). A mutant with single mutation
291 D427A and four mutants with three amino acid alanine substitutions in RBD showed
292 decreased binding to 4L12 but had no effect on 7F3 binding (Figure 7B and 7C). Even
293 though mutations F342L and E516A in the RBD region affected 7F3 neutralization,
294 they did not impact 7F3 binding, which may play an important role in ADE.

295

296 **Structures of 7F3 or 4L12 in complex with the S protein of SARS-CoV-2 revealed** 297 **different binding patterns**

298 To characterize the molecular details of the antibodies mediating ADE, we solved the
299 cryo-EM structures of S-ECD bound with 7F3 or 4L12 at an overall resolution of 3.3
300 Å and 3.0 Å, respectively (Figure S6-S8, Table S1). Details of cryo-EM sample
301 preparation, data collection and processing, as well as model building, can be found in
302 the Materials and Methods section in Supplementary Information (SI).

303 The overall resolution for S-ECD was good enough for model building, whereas the
304 resolution at the interface between 7F3 and S-ECD was worse owing to the flexibility.
305 We only docked the light chain and heavy chain of 7F3 into the cryo EM map. The S
306 protein bound with 7F3 exhibits a conformation with one “up” and two “down” RBDs,
307 among which the “up” RBD and one of two “down” RBDs were bound by 7F3, whereas
308 the other “down” RBD was not bound by 7F3 (Figure 8A). In contrast to the S/7F3
309 complex, all three RBDs of S protein were in “up” conformation and bound with 4L12
310 in the S/4L12 complex (Figure 8B). Additionally, the interfaces between antibodies and
311 RBD in both antibodies are overlapped with binding to ACE2 (Figure S9).

312 The resolution at the interface between 4L12 and RBD was improved to 3.5 Å by
313 focused refinement, allowing detailed analysis (Fig. S7). When compared with 4L12

314 bound structure, 7F3 bound to RBD with a shift of about 28.5 angstroms (Figure 8C),
315 making a different binding pattern. In summary, structural analysis indicates that both
316 7F3 and 4L12 can block the binding between ACE2 and RBD. The binding interface of
317 7F3 is accessible on the “down” RBD and is partially overlapped with the edge of the
318 receptor binding motif (RBM) (Figure 8D), which is consistent with the competing
319 results of peptides 454-473 and 484-503 (Figure 6C) and the amino acid P491A
320 substitution result (Figure 7A, B). Additionally, the epitope residues of 4L12 are
321 distributed across RBM, fully competing with ACE2 (Figure 8D). These results suggest
322 that the different ability of antibody 7F3 and 4L12 to induce ADE may result from the
323 different binding patterns to spike proteins.

324

325 **Discussion**

326 The role of antibodies during SARS-CoV-2 infection has remained unclear. For most
327 infectious viral diseases, the concentrations of virus-specific antibodies correlate with
328 viral clearance and protection, while it is different in patients of COVID-19. It was
329 reported that stronger antibody response was associated with delayed viral clearance
330 and increased disease severity in patients of COVID-19³⁰. We also reported that NAb
331 titers were higher in elderly patients of COVID-19, who tend to have worse outcomes,
332 while a few patients recovered without generating detectable NAb¹⁸. Here we reported
333 the observation of *in vitro* ADE of SARS-CoV-2 entry into FcγR2 receptor-bearing
334 cells by plasma and antibodies from patients who recovered from COVID-19. The
335 antibody enhancement of SARS-CoV-2 entry may enhance viral replication in immune
336 cells, since it has been reported that SARS-CoV-2 could productively infect immune
337 cells including monocytes and B cells both *in vivo* and *ex vivo*³¹. Because of the limited
338 availability of tissue samples from these patients, we could not directly evaluate the
339 immuno-pathological damage associated with ADE. However, in our study the
340 enhancement of virus infection was more commonly observed in plasma from older
341 patients with severe symptoms, and it was associated with prolonged disease duration,

342 suggesting that ADE may be associated with worse clinical outcomes during SARS-
343 CoV-2 infection.

344 Previous studies on SARS-CoV have shown that antibodies mediating ADE of SARS-
345 CoV infection were mainly targeting an immunodominant linear epitope (S597–603)
346 located at C-terminal domain of SARS-CoV spike protein³². Here we found that
347 antibodies mediating enhancement of SARS-CoV-2 infection were mainly targeting the
348 RBD domain of SARS-CoV-2 spike protein. The enhancement could be completely
349 blocked by pre-adsorption of RBD-specific antibodies in plasma with RBD protein. As
350 the receptor binding site of the spike protein, the RBD domain is the main target for
351 neutralizing antibodies³³. Our results indicated that some RBD-specific antibodies, for
352 example antibody 7F3 in this study, have dual effects in mediating both neutralization
353 and ADE. The effect of neutralization or ADE was dependent on receptor expression
354 on the target cells and concentration of the antibody. When viruses infect cells
355 expressing ACE2, such as Huh-7 cells or lung alveolar epithelial cells, antibody 7F3 at
356 optimal neutralizing concentration could block RBD binding to ACE2 and inhibit viral
357 infection. However, when viruses infect cells expressing Fc receptors, such as Raji,
358 K562, or primary immune cells, the antibody at suboptimal neutralizing concentration
359 promotes virus entry into cells through interaction between antibody and Fc receptors
360 (Figure 9). We found that amino acid substitutions F342L and E516A on RBD allowed
361 the virus escape from the neutralization by 7F3 without reducing binding affinity to
362 antibody. How these mutants abolished the antibody neutralization without affecting
363 binding affinity requires further studies.

364 It is interesting that antibody-mediated viral entry into Fc receptor-bearing cells was
365 not through phagocytosis, but rather, through virus-to-cell membrane fusion. However,
366 the molecular mechanism that regulates the interaction among spike protein, antibody
367 and Fc receptors in order to initiate virus-cell membrane fusion remains unknown. It
368 should be noted that not all RBD-specific antibodies will induce ADE effect. Antibodies
369 that can induce ADE in this study bind to the spike with one “up” and two “down” RBD
370 domains, while the antibodies that cannot induce ADE bind to the spike with three “up”

371 RBD domains. Therefore, the different binding pattern to spike proteins may result in
372 different abilities to promote ADE, but the detailed mechanism requires further studies.

373 Our results revealed that antibodies mediating ADE of SARS-CoV-2 infection were not
374 the result of pre-existing cross-reactive antibodies from other coronavirus infection³⁴,
375 but were generated *de novo* following infection with SARS-CoV-2. First, the plasma
376 from COVID-19 patients did not significantly promote the enhancement of SARS-CoV
377 coronavirus infection. Second, pre-incubation with SARS-CoV RBD did not block the
378 enhancement of virus infection by either plasma or monoclonal antibody 7F3. Third,
379 mAb 7F3, which promotes the enhancement of virus infection, specifically binds to
380 RBD of SARS-COV-2 virus, but no other coronaviruses. These results also suggest that
381 ADE may be more likely to occur at later time points after recovery from COVID-19
382 when the concentration of neutralizing antibodies elicited by the primary SARS-CoV-
383 2 infection have waned to suboptimal neutralizing level.

384

385 **Limitations**

386 In this study, plasma and antibodies was measured by an *in vitro* cell-based pseudovirus
387 assay to evaluate the enhancement of SARS-CoV-2 infection of immune cells. Whether
388 such enhancement of virus infection results in disease severity needs to be validated in
389 appropriate animal models.

390

391 **Implication for SARS-CoV-2 vaccine research and therapies**

392 Although several SARS-Cov-2 vaccines have been undergoing phase III clinical trials,
393 the potential ADE of coronavirus infection still remains a safety concern for any vaccine
394 candidates. The observation of enhancement of SARS-CoV-2 infection mediated by
395 plasma and antibodies from recovered COVID-19 patients in this study does not
396 indicate that vaccine candidates would necessarily induce ADE or disease severity.
397 However, these results suggest that vaccine candidates should be evaluated for

398 induction of ADE in addition to induction of neutralizing antibodies. A vaccine that can
399 induce high titers of neutralizing antibodies should be safer than one inducing low titers
400 since 1) most the newly invaded virions are neutralized before the ADE occurs and 2)
401 neutralizing antibodies mediate ADE only at the suboptimal neutralizing concentration.
402 Furthermore, these results also suggested that plasma and antibodies from patients who
403 recovered from COVID-19 should be tested for potential ADE effect before clinical
404 usage.

405

406 **Methods**

407 **Study design and participants**

408 The study was conducted under a clinical protocol approved by the Investigational
409 Review Board in the Shanghai Public Health Clinical Center (Study number: YJ-2020-
410 S018-02). The study included a cohort of 222 adult COVID-19 recovered patients who
411 were quarantined and hospitalized at the Shanghai Public Health Clinical Center. All
412 patients were diagnosed with laboratory-confirmed SARS-CoV-2 infection by positive
413 results of reverse transcriptase–polymerase chain reaction (RT-PCR) testing of
414 nasopharyngeal samples. 205 patients were categorized as mild symptoms, and 17
415 patients were in severe and critical condition according to the Guidelines on the
416 Diagnosis and Treatment of Novel Coronavirus issued by the National Health
417 Commission, China. All participants signed an informed consent approved by the IRB.
418 All patients had recovered and were discharged after meeting effective national
419 treatment standards.

420

421 **Materials**

422 The human primary embryonic kidney cell line (HEK293T) (CRL-3216™) and Raji
423 cells were obtained from the American Type Culture Collection (ATCC). 293T cells
424 expressing human angiotensin converting enzyme II (ACE2) (293 T/ACE2) were

425 constructed as previously described¹⁸. CD19+IgA-IgD-IgM- Primary B cells were
426 sorted out from peripheral blood mononuclear cell (PBMC) of recovered patients of
427 COVID-19 and expanded *in vitro* for 13 days in the presence of irradiated 3T3-msCD40L
428 feeder cells, IL-2 and IL-21 as previously described³⁵. Raji cells and K562 cells were
429 cultured in RPMI 1640 medium with 10% fetal bovine serum (FBS), and the other cells
430 were cultured in Dulbecco's Modified Eagle's Medium (DMEM) with 10% FBS.
431 HEK293 cells expressing SARS-CoV-2 RBD protein was purchased from GenScript
432 Company (Nanjing, China). SARS-CoV-2 S1 and S2 proteins, as well as SARS-CoV
433 S1 and RBD proteins were purchased from Sino Biological Company (Beijing, China).
434 The 20-mer peptides with 10 amino acid overlap spanning the entire RBD region and
435 EK1 peptide (SLDQINVTFLDLEYEMKKLEEAIAIKKLEESYIDLKEL) were
436 synthesized by Jetide (Wuhan, China). The expression plasmids for SARS S protein,
437 pcDNA3.1-SARS-S (GenBank accession: ABD72979.1), SARS-CoV-2 S protein,
438 pcDNA3.1-SARS-CoV-2-S (GenBank accession: NC_045512), and pcDNA3.1-
439 RS3367 (GenBank accession: KC881006) were synthesized by Genscript. The HIV-1
440 Env-deficient luciferase reporter vector pNL4-3. Luc. R-E- and 3T3mCD40L cells were
441 obtained through the NIH AIDS Reagent Program. Chloroquine was purchased from
442 TargetMol. Pseudoviruses of SARS-CoV-2, SARS-CoV, Bat-SL-RS3367 and WIV1
443 coronaviruses were generated by cotransfection of 293T cells with pNL4-3.Luc.R-E-
444 backbone and viral envelope protein expression plasmids as previously described¹⁸.
445 Mouse anti-human CD32 monoclonal antibody (clone number FLI8.26) was purchased
446 from BD Pharmingen (USA).

447

448 **ADE of pseudotyped SARS-CoV-2 infection of Raji cells, K562 cells, and primary** 449 **B cells**

450 The ADE effect of plasma and antibodies was measured by *in vitro* enhancement of
451 pseudotyped SARS-CoV-2 infection with Raji cells, K562 cells and primary B cells.
452 Briefly, 50 μ l of Raji cells or K562 cells were seeded into a 96-well plate pre-coated

453 with 100 μ l of 0.1 mg/ml Poly L-lysine at a concentration of 2×10^4 cells per well and
454 cultured at 37 °C for 48 hours. For primary B cells ADE assay, 100 μ l of cultured B
455 cells were seeded into wells at a concentration of 1×10^4 cells per well in the presence
456 of irradiated 3T3-msCD40L feeder cells, IL-2, and IL-21 and cultured at 37 °C for 48
457 hours. Ten μ l of heat-inactivated plasma were two-fold serially diluted with DMEM
458 with 10% FBS and mixed with 40 μ l pseudovirus at 37 °C for 30 minutes. For ADE
459 inhibition assay, different concentrations of RBD or S1 protein from SARS-CoV-2,
460 RBD or S1 protein from SARS-CoV, 20-mer peptides spanning RBD region (20 μ g/ml),
461 EK1 peptide (50 μ M), or chloroquine (50 μ M), or mouse anti-human CD32 monoclonal
462 antibody (5 μ g/ml) were incubated with serially diluted patient plasma at 37 °C for 1
463 hour before mixing with pseudovirus. The mixture was added into cultured cells for
464 infection. After 12 hours, 150 μ l of culture medium were added to the cells and
465 incubated for an additional 48 hours. The infection of cells was evaluated by luciferase
466 expression, as determined with a luciferase assay system (Promega) and read on a
467 luminometer (Perkin Elmer). The enhancement of virus infection was expressed as the
468 fold changes of luciferase reading comparing to virus control without addition of
469 plasma or antibodies.

470

471 **Purification of IgG from human plasma**

472 Heat-inactivated human plasma samples were 1:6 diluted in PBS and filtered through
473 0.22 μ m filters. The diluted plasma was incubated with protein G beads (Smart-
474 Lifesciences) at 4 °C overnight. The mixture was loaded on filtration column, and IgG-
475 depleted plasma was collected from the flow through. After washing with 150 ml PBS,
476 the beads binding IgG were eluted with 8 ml of 0.1M glycine-HCl buffer (pH 2.7) and
477 neutralized with 200 μ l of 2 M Tris-HCl buffer (pH 8.0). The eluted IgG was
478 concentrated using Amicon Ultra centrifugation units (50 kDa, Millipore) after triple
479 washing with 15 ml PBS. Purified IgG was diluted with PBS to the same volume as
480 that of the original plasma samples before evaluation.

481

482 **Neutralization assay**

483 Neutralization activity of plasma and antibodies was measured by the inhibition of
484 pseudovirus infection with 293 T/ACE2 cells as previously described¹⁸. Briefly,
485 293 T/ACE2 cells were seeded in a 96-well plate at a concentration of 10^4 cells per well
486 and cultured for 12 hours. Then, ten μ l heat-inactivated plasma were five-fold serially
487 diluted with DMEM with 10% FBS and mixed with 40 μ l of pseudovirus. The mixture
488 was added to cultured 293 T/ACE2 cells for infection. The culture medium was
489 refreshed after 12 hours and incubated for an additional 48 hours. Assays were
490 developed with a luciferase assay system (Promega), and the relative light units (RLU)
491 were read on a luminometer (Perkin Elmer). The titers of NAbs were calculated as 50%
492 inhibitory dose (ID₅₀), expressed as the highest dilution of plasma which resulted in a
493 50% reduction of luciferase luminescence compared with virus control.

494

495 **Cell-cell fusion assay mediated by ADE patient plasma.**

496 Cell-cell fusion assay was conducted as previously described with modification²⁷.
497 Briefly, HEK-293T cells expressing the SARS-CoV-2 S protein on the cell membrane
498 were used as effector cells, while Raji cells were used as target cells. HEK293T cells
499 were transfected with plasmid pAAV-IRES-EGFP-SARS-2-S, using transfection
500 reagent VigoFect (Vigorous Biotechnology, China). Raji cells were seeded at a density
501 of 5×10^4 cells per well into the 96-well plates which were precoated with 100 μ l of 0.1
502 mg/ml of Poly L-lysine for 30 min at 37°C. The effector cells were collected 24 hours
503 after transfection and mixed with the serially diluted serum at 37°C for 30 min. The
504 mixture of effector cells and serum was applied onto the Raji cells and cultured for an
505 additional 24 hours. After fixing with 4 % paraformaldehyde, the cells were observed
506 and captured using an inverted fluorescence microscope (Nikon Eclipse Ti-S). The
507 fused cells were counted on five random fields in each well. For inhibition assay, EK1
508 peptide or chloroquine (TargetMol) was two-fold serially diluted in RPMI 1640 and

509 then mixed with the effector cells and serially diluted ADE patient plasma at 37°C for
510 30 min. Then, the mixture was applied to the Raji cell as described above.

511

512 **ELISA**

513 SARS-CoV-2 RBD, S1, or S2 protein were coated on a MaxiSorp Nunc-immuno 96-
514 well plate (Thermo Scientific, USA) overnight at 4 °C. Wells were blocked with 5%
515 nonfat milk (Biofroxx, Germany) in PBS for 1 hour at room temperature, followed by
516 incubation with 1:400 diluted sera or serially diluted sera in disruption buffer (PBS, 5%
517 FBS, 2% BSA, and 1% Tween-20) for 1 hour at room temperature. A 1:2500 dilution
518 of horseradish peroxidase (HRP)-conjugated goat anti-human IgG antibody (Jackson
519 Immuno Research Laboratories, USA) was added for 1 hour at room temperature. Wells
520 were developed using ABST (Thermo Scientific, USA) for 30 minutes and read at 405
521 nm on a Multiskan FC plate reader (Thermo Scientific, USA).

522

523 **Memory B-cell staining, sorting and antibody cloning**

524 SARS-CoV-2-specific monoclonal antibodies were isolated from mononuclear cells
525 (PBMC) of recovered patients by *in vitro* single B cell as previously described³⁵. Briefly,
526 CD19⁺IgA⁻IgD⁻IgM⁻ memory B cells were sorted and resuspended in medium with
527 IL-2, IL-21, and irradiated 3T3-msCD40L feeder cells, followed by seeding into 384-
528 well plates at a density of 4 cells per well. After 13 days of incubation, supernatants
529 from each well were screened for neutralization activity using a high-throughput micro-
530 neutralization assay against SARS-CoV-2. From the wells that scored positive in the
531 neutralization assay, the variable region of the heavy chain and the light chain of the
532 immunoglobulin gene was amplified by RT-PCR and re-expressed as described
533 previously^{36,37}. The full-length IgG was purified using a protein G column (Smart-
534 Lifesciences).

535

536 **Biolayer interferometry binding assay**

537 The kinetics of monoclonal antibody binding to SARS-CoV-2 RBD protein was
538 measured by biolayer interferometry binding assay on a FortéBio OctetRED96
539 instrument using anti-human IgG (AHC) biosensors as previously described³⁸ The
540 assay followed sequential steps at 30°C as follows. First, the biosensor was immersed
541 in sterile water for 60s, and 10 µg/ml of antibody was loaded on the biosensors. The
542 biosensors were dipped into 0.02% PBST (PBS with 0.02% Tween) for 300 s to reach
543 baseline and then incubated with serially diluted RBD protein solutions for association
544 and PBST for dissociation. Results were analyzed, and K_{on} , K_{off} and KD were calculated
545 by FortéBio Data Analysis software (Version 8.1) using 1:1 binding and a global fitting
546 model.

547

548 **Cryo-EM sample preparation**

549 The peak fractions of complex were concentrated to about 1.5 mg/mL and applied to
550 the grids. Aliquots (3.3 µL) of the protein complex were placed on glow-discharged
551 holey carbon grids (Quantifoil Au R1.2/1.3). The grids were blotted for 2.5 s or 3.0 s
552 and flash-frozen in liquid ethane cooled by liquid nitrogen with Vitrobot (Mark IV,
553 Thermo Scientific). The cryo-EM samples were transferred to a Titan Krios operating
554 at 300 kV equipped with Cs corrector, Gatan K3 Summit detector and GIF Quantum
555 energy filter. Movie stacks were automatically collected using AutoEMation³⁹, with a
556 slit width of 20 eV on the energy filter and a defocus range from -1.2 µm to -2.2 µm in
557 super-resolution mode at a nominal magnification of 81,000×. Each stack was exposed
558 for 2.56 s with an exposure time of 0.08 s per frame, resulting in a total of 32 frames
559 per stack. The total dose rate was approximately 50 e⁻/Å² for each stack. The stacks
560 were motion corrected with MotionCor2⁴⁰ and binned 2-fold, resulting in a pixel size
561 of 1.087 Å/pixel. Meanwhile, dose weighting was performed⁴¹. The defocus values
562 were estimated with Gctf⁴².

563

564 **Data processing**

565 Particles for all samples were automatically picked using Relion 3.0.6⁴³⁻⁴⁶ from

566 manually selected micrographs. After 2D classification with Relion, good particles
567 were selected and subjected to two cycles of heterogeneous refinement without
568 symmetry using cryoSPARC⁴⁷. The good particles were selected and subjected to Non-
569 uniform Refinement (beta) with C1 symmetry, resulting in 3D reconstruction for the
570 whole structures, which were further subjected to 3D auto-refinement and post-
571 processing with Relion. For interface between SARS-CoV-2 S protein and mAb, the
572 dataset was subjected to focused refinement with adapted mask on each RBD-mAb sub-
573 complex to improve map quality. Then the datasets of three similar RBD-mAb sub-
574 complexes were combined and subjected to focused refinement with Relion. The
575 combined dataset was recentered on the interface between RBD and mAb and re-
576 extracted. The re-extracted dataset was 3D classified with Relion focused on RBD-mAb
577 sub-complex. Then the good particles were selected and subjected to focused
578 refinement with Relion, resulting in 3D reconstruction of better quality on the RBD-
579 mAb sub-complex.

580 The resolution was estimated with the gold-standard Fourier shell correlation 0.143
581 criterion⁴⁸ with high-resolution noise substitution⁴⁹. Refer to Supplemental Figures
582 S6-S7 and Supplemental Table S1 for details of data collection and processing.

583

584 **Model building and structure refinement**

585 For model building of all complexes of S-ECD of SARS-CoV-2 with mAb, atomic
586 models (PDB ID: 7C2L) were used as templates, which were molecular dynamics
587 flexible fitted⁵⁰ into the whole cryo-EM map of the complex and the focused-refined
588 cryo-EM map of the RBD-mAb sub-complex, respectively. The fitted atomic models
589 were further manually adjusted with Coot⁵¹. Each residue was manually checked with
590 the chemical properties taken into consideration during model building. Several
591 segments were not modeled because the corresponding densities were invisible.
592 Structural refinement was performed in Phenix⁵² with secondary structure and
593 geometry restraints to prevent overfitting. To monitor the potential overfitting, the
594 model was refined against one of the two independent half maps from the gold standard

595 3D refinement approach. Then, the refined model was tested against the other maps.
596 Statistics associated with data collection, 3D reconstruction, and model building were
597 summarized in Table S1.

598

599 **Statistical analysis**

600 Statistical analyses were carried out using GraphPad Prism 7.0. Data are indicated as
601 median [IQR]. Differences between nominal data were tested for statistical significance
602 by use of Nonparametric paired or unpaired *t* test. Kruskal-Wallis test was used to
603 compare the differences between three or more groups, and Dunn's multiple
604 comparisons test was used to correct for multiple comparisons. All tests were two-tailed,
605 and $P < .05$ was considered statistically significant.

606 **Role of the funding source**

607 The funders of the study had no role in study design, data collection, data analysis, data
608 interpretation, or writing of the report. The corresponding authors had full access to all
609 data in the study and had final responsibility for the decision to submit for publication.

610

611 **Declaration of interests**

612 Patents about the monoclonal antibodies 7F3 and 4L12 in this study are pending.

613

614 **Contributions**

615 JH, FW, QZ, LL conceived and designed the experiments. ZS, YZ, and TZ collected
616 the samples and clinical information of patients. JH, ML and FW performed ADE
617 experiments, blocking experiments, peptide array, neutralization assay, ELISA,
618 memory B-cell staining, sorting, and antibody cloning. RY, QZ, ZY and LY performed
619 the structural studies. ZL and LL performed cell-cell fusion assay and blocking assay.
620 YDW, TS, XL, ZL, CL, and TY constructed and expressed SARS-CoV-2 pseudovirus
621 mutants and RBD-Fc protein mutants. YDW, YLW, and JH performed biolayer

622 interferometry binding assay. YDW and YM performed ELISA. DL and YM
623 contributed to ADE experiment. KW, DL, and QW expressed SARS-CoV-2
624 pseudovirus and their mutants and purification antibodies. PJ contributed to B cell
625 sorting. This project was supervised by YZ, TZ, JS, and YMW. JH, FW, QZ, LL, RY,
626 ML, ZL, and YDW analyzed the data and wrote the manuscript.

627

628 **Acknowledgments**

629 We thank Prof. Zhengli Shi for helpful discussion and thank Dr. Vanessa M. Hirsch in
630 NIH, USA for reviewing this manuscript. This work was supported by the National
631 Natural Science Foundation of China (31771008 to JH, 31930001 to YZ and FW,
632 82041025 to SJ, and 31971123 to QZ), the National Major Science and Technology
633 Projects of China (2017ZX10202102 to JH and 2018ZX10301403 to FW and
634 LL), Hundred Talent Program of Shanghai Municipal Health Commission (2018BR08
635 to JH), Chinese Academy of Medical Sciences (2019PT350002 to JH), Program of
636 Shanghai Academic/Technology Research Leader (20XD1420300 to LL), the Key
637 R&D Program of Zhejiang Province (2020C04001), the SARS-CoV-2 Emergency
638 Project of the Science and Technology Department of Zhejiang Province (2020C03129),
639 the Leading Innovative and Entrepreneur Team Introduction Program of Hangzhou, and
640 the Special Research Program of Novel Coronavirus Pneumonia of Westlake University
641 and Tencent foundation to QZ. We thank all healthcare personnel and staff in the BSL3
642 lab involved in the collection of patients' samples at the Shanghai Public Health Clinical
643 Center, the Cryo-EM Facility and Supercomputer Center of Westlake University for
644 providing cryo-EM and computation support and members of the Core Facility of
645 Microbiology and Parasitology (SHMC) of Fudan University, especially Qian Wang for
646 technical support.

647

648 **References**

- 649 1 *Coronavirus disease (COVID-19) Weekly Epidemiological Update and Weekly Operational*
650 *Update*, <[https://www.who.int/emergencies/diseases/novel-coronavirus-2019/situation-](https://www.who.int/emergencies/diseases/novel-coronavirus-2019/situation-reports/)
651 [reports/](https://www.who.int/emergencies/diseases/novel-coronavirus-2019/situation-reports/)> (
652 2 *Draft landscape of COVID-19 candidate vaccines*,
653 <[https://www.who.int/publications/m/item/draft-landscape-of-covid-19-candidate-](https://www.who.int/publications/m/item/draft-landscape-of-covid-19-candidate-vaccines)
654 [vaccines](https://www.who.int/publications/m/item/draft-landscape-of-covid-19-candidate-vaccines)> (
655 3 Yang, J. *et al.* A vaccine targeting the RBD of the S protein of SARS-CoV-2 induces
656 protective immunity. *Nature*, doi:10.1038/s41586-020-2599-8 (2020).
657 4 Zhu, F. C. *et al.* Immunogenicity and safety of a recombinant adenovirus type-5-vectored
658 COVID-19 vaccine in healthy adults aged 18 years or older: a randomised, double-blind,
659 placebo-controlled, phase 2 trial. *Lancet* **396**, 479-488, doi:10.1016/S0140-
660 6736(20)31605-6 (2020).
661 5 Yu, J. *et al.* DNA vaccine protection against SARS-CoV-2 in rhesus macaques. *Science* **369**,
662 806-811, doi:10.1126/science.abc6284 (2020).

- 663 6 Folegatti, P. M. *et al.* Safety and immunogenicity of the ChAdOx1 nCoV-19 vaccine against
664 SARS-CoV-2: a preliminary report of a phase 1/2, single-blind, randomised controlled
665 trial. *Lancet* **396**, 467-478, doi:10.1016/S0140-6736(20)31604-4 (2020).
- 666 7 Liu, L. *et al.* Anti-spike IgG causes severe acute lung injury by skewing macrophage
667 responses during acute SARS-CoV infection. *JCI Insight* **4**, doi:10.1172/jci.insight.123158
668 (2019).
- 669 8 Honda-Okubo, Y. *et al.* Severe acute respiratory syndrome-associated coronavirus
670 vaccines formulated with delta inulin adjuvants provide enhanced protection while
671 ameliorating lung eosinophilic immunopathology. *J Virol* **89**, 2995-3007,
672 doi:10.1128/JVI.02980-14 (2015).
- 673 9 Hashem, A. M. *et al.* A Highly Immunogenic, Protective, and Safe Adenovirus-Based
674 Vaccine Expressing Middle East Respiratory Syndrome Coronavirus S1-CD40L Fusion
675 Protein in a Transgenic Human Dipeptidyl Peptidase 4 Mouse Model. *J Infect Dis* **220**,
676 1558-1567, doi:10.1093/infdis/jiz137 (2019).
- 677 10 Agrawal, A. S. *et al.* Immunization with inactivated Middle East Respiratory Syndrome
678 coronavirus vaccine leads to lung immunopathology on challenge with live virus. *Hum*
679 *Vaccin Immunother* **12**, 2351-2356, doi:10.1080/21645515.2016.1177688 (2016).
- 680 11 Jiang, S. Don't rush to deploy COVID-19 vaccines and drugs without sufficient safety
681 guarantees. *Nature* **579**, 321, doi:10.1038/d41586-020-00751-9 (2020).
- 682 12 Tirado, S. M. & Yoon, K. J. Antibody-dependent enhancement of virus infection and
683 disease. *Viral Immunol* **16**, 69-86, doi:10.1089/088282403763635465 (2003).
- 684 13 Taylor, A. *et al.* Fc receptors in antibody-dependent enhancement of viral infections.
685 *Immunol Rev* **268**, 340-364, doi:10.1111/imr.12367 (2015).
- 686 14 Katzelnick, L. C. *et al.* Antibody-dependent enhancement of severe dengue disease in
687 humans. *Science* **358**, 929-932, doi:10.1126/science.aan6836 (2017).
- 688 15 Bardina, S. V. *et al.* Enhancement of Zika virus pathogenesis by preexisting antinflavirus
689 immunity. *Science* **356**, 175-180, doi:10.1126/science.aal4365 (2017).
- 690 16 Halstead, S. B. Neutralization and antibody-dependent enhancement of dengue viruses.
691 *Adv Virus Res* **60**, 421-467, doi:10.1016/s0065-3527(03)60011-4 (2003).
- 692 17 Vennema, H. *et al.* Early death after feline infectious peritonitis virus challenge due to
693 recombinant vaccinia virus immunization. *J Virol* **64**, 1407-1409,
694 doi:10.1128/JVI.64.3.1407-1409.1990 (1990).
- 695 18 Wu, F. *et al.* Evaluating the Association of Clinical Characteristics With Neutralizing
696 Antibody Levels in Patients Who Have Recovered From Mild COVID-19 in Shanghai, China.
697 *JAMA Intern Med*, doi:10.1001/jamainternmed.2020.4616 (2020).
- 698 19 Long, Q. X. *et al.* Antibody responses to SARS-CoV-2 in patients with COVID-19. *Nat Med*
699 **26**, 845-848, doi:10.1038/s41591-020-0897-1 (2020).
- 700 20 Arvin, A. M. *et al.* A perspective on potential antibody-dependent enhancement of SARS-
701 CoV-2. *Nature* **584**, 353-363, doi:10.1038/s41586-020-2538-8 (2020).
- 702 21 Sariol, A. & Perlman, S. Lessons for COVID-19 Immunity from Other Coronavirus
703 Infections. *Immunity* **53**, 248-263, doi:10.1016/j.immuni.2020.07.005 (2020).
- 704 22 Shen, C. *et al.* Treatment of 5 Critically Ill Patients With COVID-19 With Convalescent
705 Plasma. *JAMA* **323**, 1582-1589, doi:10.1001/jama.2020.4783 (2020).

- 706 23 Administration, U. F. a. D. *Recommendations for Investigational COVID-19 Convalescent*
707 *Plasma*, <[https://www.fda.gov/vaccines-blood-biologics/investigational-new-drug-ind-](https://www.fda.gov/vaccines-blood-biologics/investigational-new-drug-ind-or-device-exemption-ide-process-cber/recommendations-investigational-covid-19-convalescent-plasma)
708 [or-device-exemption-ide-process-cber/recommendations-investigational-covid-19-](https://www.fda.gov/vaccines-blood-biologics/investigational-new-drug-ind-or-device-exemption-ide-process-cber/recommendations-investigational-covid-19-convalescent-plasma)
709 [convalescent-plasma](https://www.fda.gov/vaccines-blood-biologics/investigational-new-drug-ind-or-device-exemption-ide-process-cber/recommendations-investigational-covid-19-convalescent-plasma)> (
710 24 Jaume, M. *et al.* Anti-severe acute respiratory syndrome coronavirus spike antibodies
711 trigger infection of human immune cells via a pH- and cysteine protease-independent
712 FcγR pathway. *J Virol* **85**, 10582-10597, doi:10.1128/JVI.00671-11 (2011).
713 25 Bournazos, S., Gupta, A. & Ravetch, J. V. The role of IgG Fc receptors in antibody-
714 dependent enhancement. *Nat Rev Immunol*, doi:10.1038/s41577-020-00410-0 (2020).
715 26 Byrd, T. F. & Horwitz, M. A. Chloroquine inhibits the intracellular multiplication of
716 *Legionella pneumophila* by limiting the availability of iron. A potential new mechanism for
717 the therapeutic effect of chloroquine against intracellular pathogens. *J Clin Invest* **88**, 351-
718 357, doi:10.1172/JCI115301 (1991).
719 27 Xia, S. *et al.* Inhibition of SARS-CoV-2 (previously 2019-nCoV) infection by a highly potent
720 pan-coronavirus fusion inhibitor targeting its spike protein that harbors a high capacity
721 to mediate membrane fusion. *Cell Res* **30**, 343-355, doi:10.1038/s41422-020-0305-x
722 (2020).
723 28 Li, Q. *et al.* The Impact of Mutations in SARS-CoV-2 Spike on Viral Infectivity and
724 Antigenicity. *Cell* **182**, 1284-1294 e1289, doi:10.1016/j.cell.2020.07.012 (2020).
725 29 Korber, B. *et al.* Tracking Changes in SARS-CoV-2 Spike: Evidence that D614G Increases
726 Infectivity of the COVID-19 Virus. *Cell* **182**, 812-827 e819, doi:10.1016/j.cell.2020.06.043
727 (2020).
728 30 Zhao, J. *et al.* Antibody responses to SARS-CoV-2 in patients of novel coronavirus disease
729 2019. *Clin Infect Dis*, doi:10.1093/cid/ciaa344 (2020).
730 31 Pontelli, M. *et al.* Infection of human lymphomononuclear cells by SARS-CoV-2. *bioRxiv*,
731 doi:doi:10.1101/2020.07.28.225912 (2020).
732 32 Wang, Q. *et al.* Immunodominant SARS Coronavirus Epitopes in Humans Elicited both
733 Enhancing and Neutralizing Effects on Infection in Non-human Primates. *ACS Infect Dis*
734 **2**, 361-376, doi:10.1021/acsinfecdis.6b00006 (2016).
735 33 Du, L. *et al.* The spike protein of SARS-CoV-2 a target for vaccine and therapeutic
736 development. *Nat Rev Microbiol* **7**, 226-236, doi:10.1038/nrmicro2090 (2009).
737 34 Tetro, J. A. Is COVID-19 receiving ADE from other coronaviruses? *Microbes Infect* **22**, 72-
738 73, doi:10.1016/j.micinf.2020.02.006 (2020).
739 35 Huang, J. *et al.* Isolation of human monoclonal antibodies from peripheral blood B cells.
740 *Nat Protoc* **8**, 1907-1915, doi:10.1038/nprot.2013.117 (2013).
741 36 Tiller, T. *et al.* Efficient generation of monoclonal antibodies from single human B cells by
742 single cell RT-PCR and expression vector cloning. *Journal of immunological methods* **329**,
743 112-124, doi:10.1016/j.jim.2007.09.017 (2008).
744 37 Georgiev, I. S. *et al.* Delineating antibody recognition in polyclonal sera from patterns of
745 HIV-1-isolate neutralization. *Science*, in press (2013).
746 38 Tian, X. *et al.* Potent binding of 2019 novel coronavirus spike protein by a SARS
747 coronavirus-specific human monoclonal antibody. *Emerg Microbes Infect* **9**, 382-385,
748 doi:10.1080/22221751.2020.1729069 (2020).
749 39 Lei, J. & Frank, J. Automated acquisition of cryo-electron micrographs for single particle

- 750 reconstruction on an FEI Tecnai electron microscope. *Journal of structural biology* **150**,
751 69-80, doi:10.1016/j.jsb.2005.01.002 (2005).
- 752 40 Zheng, S. Q. *et al.* MotionCor2: anisotropic correction of beam-induced motion for
753 improved cryo-electron microscopy. *Nature methods* **14**, 331-332,
754 doi:10.1038/nmeth.4193 (2017).
- 755 41 Grant, T. & Grigorieff, N. Measuring the optimal exposure for single particle cryo-EM using
756 a 2.6 Å reconstruction of rotavirus VP6. *eLife* **4**, e06980, doi:10.7554/eLife.06980 (2015).
- 757 42 Zhang, K. Gctf: Real-time CTF determination and correction. *Journal of structural biology*
758 **193**, 1-12, doi:10.1016/j.jsb.2015.11.003 (2016).
- 759 43 Zivanov, J. *et al.* New tools for automated high-resolution cryo-EM structure
760 determination in RELION-3. *eLife* **7**, doi:10.7554/eLife.42166 (2018).
- 761 44 Kimanius, D., Forsberg, B. O., Scheres, S. H. & Lindahl, E. Accelerated cryo-EM structure
762 determination with parallelisation using GPUs in RELION-2. *eLife* **5**,
763 doi:10.7554/eLife.18722 (2016).
- 764 45 Scheres, S. H. RELION: implementation of a Bayesian approach to cryo-EM structure
765 determination. *Journal of structural biology* **180**, 519-530, doi:10.1016/j.jsb.2012.09.006
766 (2012).
- 767 46 Scheres, S. H. A Bayesian view on cryo-EM structure determination. *Journal of molecular*
768 *biology* **415**, 406-418, doi:10.1016/j.jmb.2011.11.010 (2012).
- 769 47 Punjani, A., Rubinstein, J. L., Fleet, D. J. & Brubaker, M. A. cryoSPARC: algorithms for rapid
770 unsupervised cryo-EM structure determination. *Nature methods* **14**, 290-296,
771 doi:10.1038/nmeth.4169 (2017).
- 772 48 Rosenthal, P. B. & Henderson, R. Optimal determination of particle orientation, absolute
773 hand, and contrast loss in single-particle electron cryomicroscopy. *Journal of molecular*
774 *biology* **333**, 721-745 (2003).
- 775 49 Chen, S. *et al.* High-resolution noise substitution to measure overfitting and validate
776 resolution in 3D structure determination by single particle electron cryomicroscopy.
777 *Ultramicroscopy* **135**, 24-35, doi:10.1016/j.ultramic.2013.06.004 (2013).
- 778 50 Trabuco, L. G., Villa, E., Mitra, K., Frank, J. & Schulten, K. Flexible fitting of atomic structures
779 into electron microscopy maps using molecular dynamics. *Structure (London, England :
780 1993)* **16**, 673-683, doi:10.1016/j.str.2008.03.005 (2008).
- 781 51 Emsley, P., Lohkamp, B., Scott, W. G. & Cowtan, K. Features and development of Coot.
782 *Acta crystallographica. Section D, Biological crystallography* **66**, 486-501,
783 doi:10.1107/S0907444910007493 (2010).
- 784 52 Adams, P. D. *et al.* PHENIX: a comprehensive Python-based system for macromolecular
785 structure solution. *Acta crystallographica. Section D, Biological crystallography* **66**, 213-
786 221, doi:10.1107/S0907444909052925 (2010).

787

788

789 **Figure legends**

790 **Figure 1. Plasma from 8% of the recovered patients with mild COVID-19 and 76% of the recovered**
791 **patients with severe COVID-19 showed enhancement of SARS-CoV-2 infection through IgG Fc**
792 **with the engagement of FcR2 receptor.**

793 (A) Clinical characteristics of COVID-19 recovered patients whose plasma showed ADE. (B) The
794 enhancement of SARS-CoV-2, SARS-CoV, SARS-related RS3367, WIV-1 infection of Raji cells by 29
795 plasma samples from patients who recovered from mild COVID-19 (N=16, blue) or severe COVID-19
796 (N=13, red) are shown. Plasma from 10 uninfected donors was used as negative controls. For each plasma
797 sample, the area under curve (AUC) of fold changes of enhancement was calculated. (C) The
798 enhancement of SARS-CoV-2 infection of K562 cells by 29 plasma samples are shown. (D) The
799 enhancement of SARS-CoV-2 infection of primary B cells by eight representative plasma samples are
800 shown. (E) ADE of SARS-CoV-2 infection was mediated by plasma IgG with the engagement of FcγRII
801 receptor. IgG purified from the ADE plasma was evaluated for enhancement of SARS-CoV-2 infection
802 of Raji cells. IgG-depleted plasma was also evaluated. (F) ADE plasma or (G) IgG purified from ADE
803 plasma (right) were evaluated for ADE on Raji cells in the presence or absence of anti-FcγRII antibody
804 CD32. Comparison of age (H), disease duration (I), and hospital stay (J) of 29 patients whose plasma
805 showed ADE effect and 193 patients whose plasma did not show ADE effect (green). P value was
806 calculated using non-parametric *t* test.

807

808 **Figure 2. ADE is more likely to develop in elderly patients with high titers of SARS-CoV-2 RBD-**
809 **and S1-specific antibodies.**

810 (A) SARS-CoV-2 NAb titers (ID50) and (B) RBD, S1-, and S2-specific binding antibodies of 29 ADE
811 patients and 193 Non-ADE patients are compared. P value was calculated using *t* test. (C) Kinetics of
812 SARS-CoV-2-specific ADE in plasma of six COVID-19 patients are shown. Plasma was collected at
813 different time points post-disease onset. (D) Kinetics of spike-binding antibodies (left Y axis) targeting
814 RBD, S1, and S2 in plasma of six COVID-19 patients exhibiting ADE are shown. Plasma diluted 1:400
815 was incubated with RBD, S1, or S2 protein. (E) Kinetics of SARS-CoV-2 NAb titers in plasma of six
816 COVID-19 patients whose plasma showed ADE are shown.

817

818 **Figure 3. ADE was mediated by antibodies binding to SARS-CoV-2 spike RBD subunits.**

819 (A) Suppression of ADE of plasma by RBD (A) or S1 protein (B) of SARS-CoV-2 but not by RBD (C)
820 or S1 protein (D) of SARS-CoV viruses. Serially diluted patient plasma were pre-incubated with different
821 concentrations of proteins before evaluating ADE of SARS-CoV-2 infection of Raji cells. Untreated
822 plasma was used as a positive control, and healthy donor plasma was used as a negative control. (E) ADE
823 mediated by plasma from six patients was inhibited by pre-incubation with 10 μg/ml SARS-CoV-2 RBD
824 but not SARS-CoV RBD.

825

826 **Figure 4. ADE-mediated SARS-CoV-2 entry into cells is through virus-cell membrane fusion.**

827 Inhibition of ADE induced by plasma from patients using chloroquine (A) or EK peptide (B). Serially
828 diluted plasma was pre-incubated with different concentrations of chloroquine or EK1 peptide before
829 evaluating ADE of SARS-CoV-2 infection of Raji cells. Patient plasma with ADE was used as a positive
830 control, and plasma from uninfected health donor was used as a negative control. (C) ADE mediated by
831 plasma from six patients was inhibited by 50 μM of EK1 peptide but not by chloroquine.. (D) ADE
832 plasma from recovered COVID-19 patients promoted syncytium formation. Plasma from uninfected
833 health donor was used as a negative control. The syncytium formation was specifically inhibited by EK1
834 peptide but not by chloroquine. (E) The statistical counts of syncytium formation induced by plasma
835 from three patients (8, 5, and 7) in the presence of EK1 peptide or chloroquine.

836

837 **Figure 5. RBD-specific NAb 7F3 from a recovered patient of COVID-19 enhanced SARS-CoV-2**
838 **entry into cells through virus-cell membrane fusion.**

839 (A) Neutralizing curve of 7F3 and 4L12 against SARS-CoV-2 pseudovirus. (B) Binding of 7F3 and 4L12
840 mAb to SARS-CoV-2 RBD, S1, and S2 proteins in ELISA assay. (C) Binding affinity of 7F3 and 4L12
841 to RBD was measured by bilayer interferometry experiments. (D) Enhancement of SARS-CoV-2
842 infection of Raji cells by 7F3 but not by 4L12. (E) Impact of IgG, Fab, and Fc of 7F3 on ADE of SARS-
843 CoV-2 infection. (F) Impact of IgG1, IgG2, IgG3, and IgG4 isotypes of 7F3 on ADE of SARS-CoV-2
844 infection. (G) Blockage of RcrRII with anti-CD32 antibody (5 µg/mL) inhibited ADE induced by 7F3.
845 (H) RBD of SARS-CoV-2 (left) blocked ADE induced by 7F3. RBD of SARS-CoV (right) was used as
846 a negative control. (I) Blockage of ADE induced by 7F3 with EK1 (left) and chloroquine (right).

847

848 **Figure 6. Peptide scanning for hot spots in RBD associated with ADE effect.**

849 ADE of patient plasma (A) and antibody 7F3 (B) were blocked with 20-mer overlapping peptides
850 covering RBD protein. Serially diluted ADE patient plasma was pre-incubated with 20 µg/ml peptides
851 before evaluating ADE effect on Raji cells. Patient plasma with ADE was used as a positive control, and
852 plasma from uninfected health donor was used as a negative control. (C) Percentage of AUC changes of
853 ADE curves after blocking of ADE patient plasma and 7F3 with 20-mer RBD overlapping peptides.

854

855 **Figure 7. ADE antibody 7F3 and non-ADE antibody 4L12 shared overlapping epitopes but showed**
856 **different binding abilities to RBD.**

857 (A) Neutralization potency and breadth of antibodies against 27 SARS-CoV-2 RBD mutants. Mutants
858 reported to be resistant to SARS-CoV-2 NAbS were highlighted in blue. (B) Percentage of 7F3 or 4L12
859 binding to SARS-CoV-2 RBD mutants compared with RBD WT. Values between 0.5 - 0.8 are highlighted
860 in yellow, and values < 0.5 are highlighted in red. (C) Binding curves of 7F3 or 4L12 to SARS-CoV-2
861 RBD and its mutants.

862

863 **Figure 8. Structures of 7F3 or 4L12 in complex with the S protein of SARS-CoV-2 revealed**
864 **different binding patterns.**

865 (A) Cryo-EM structure of the 7F3-bound S protein. 7F3 binds to one “up” RBD and one “down” RBD.
866 (B) Cryo-EM structure of the 4L12-bound S protein. The insets in (A) and (B) show the details of the
867 corresponding regions. (C) 7F3 shifts for about 28.5 angstroms compared with 4L12. (D) The ACE2
868 binding site and the epitopes of 7F3 and 4L12 on RBD of the S protein. The complexes of RBD with
869 ACE2 and the antibody 7F3 and 4L12 are shown as cartoon in left column. The RBD is shown as grey
870 surface in middle column, with the ACE2 binding site colored in green and the epitope of 7F3 and 4L12
871 colored in orange and pink, respectively. In the right column, the antibodies are shown as surface, with
872 the heavy and light chains colored as in (A) and the paratopes colored in grey.

873

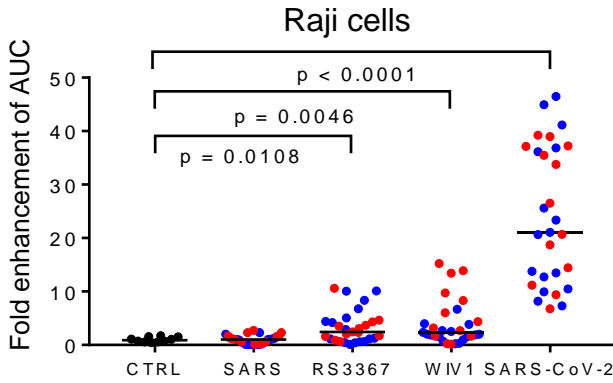
874 **Figure 9. Scheme of dual effects of SARS-CoV-2 neutralizing antibodies on mediating both**
875 **neutralization and ADE.**

876 (A) Binding of NAbS to RBD of SARS-CoV-2 spike protein blocks virus from infecting ACE2 receptor
877 expressing cells. (B) Binding of NAbS to Fc receptors (FcRs) expressing immune cells with their Fc
878 domains and to the RBD with their Fab domains triggers fusion-based viral infection.

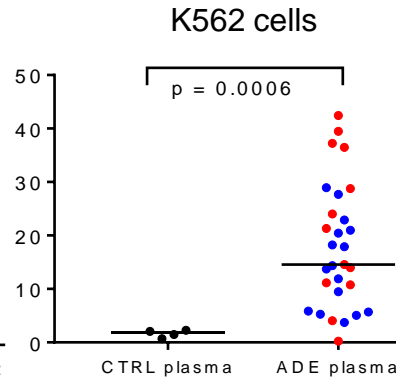
A

| Patient Information | Mild COVID-19 | | | Severe COVID-19 | | | All patients |
|-------------------------|---------------|------------|------------|-----------------|------------|------------|--------------|
| | Total | Non-ADE | ADE | Total | Non-ADE | ADE | |
| Patient No. (%) | 205 (100) | 189 (92) | 16 (8) | 17 (100) | 4 (24) | 13 (76) | 222 |
| Male (%) | 102 (50) | 97 (47) | 5 (3) | 12 (70) | 2 (12) | 10 (58) | 114 |
| Female (%) | 103 (50) | 92 (45) | 11 (5) | 5 (30) | 2 (12) | 3 (18) | 108 |
| Median Age (Years) | 51 [37-64] | 50 [37-63] | 63 [44-66] | 66 [64-78] | 66 [64-70] | 69 [64-80] | 53 [38-65] |
| Length of stay (days) | 17 [13-23] | 16 [13-22] | 20 [16-26] | 50 [33-72] | 27 [25-32] | 57 [40-75] | 17 [13-24] |
| Disease duration (days) | 22 [18-29] | 22 [18-28] | 25 [22-31] | 58 [39-75] | 32 [30-37] | 61 [46-79] | 23 [18-30] |

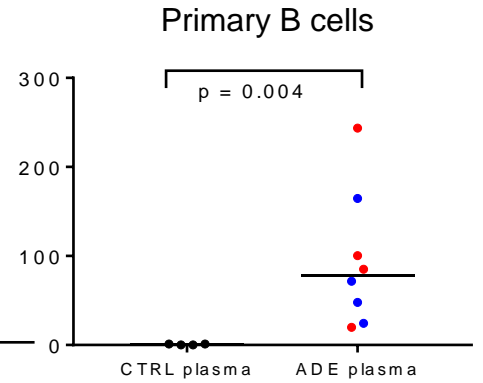
B



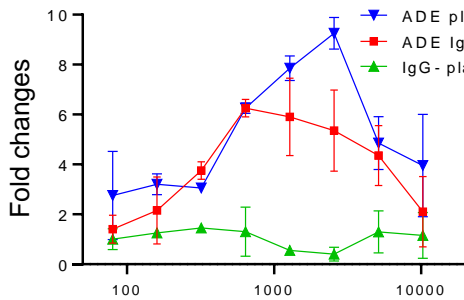
C



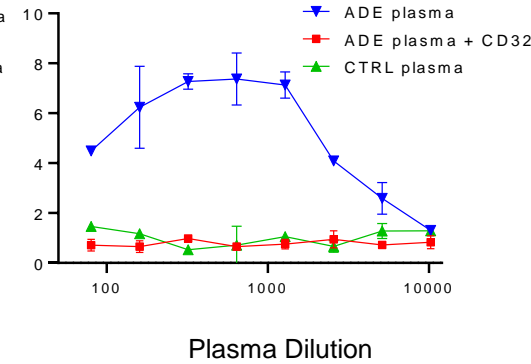
D



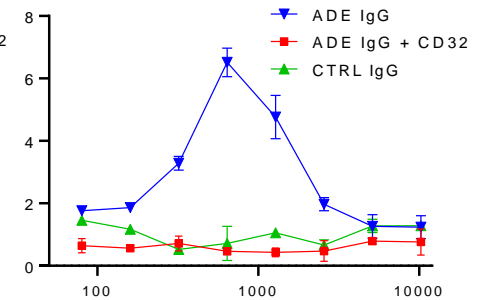
E



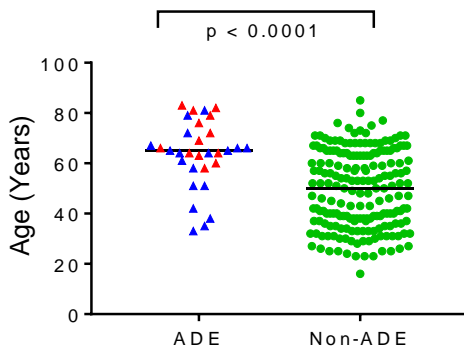
F



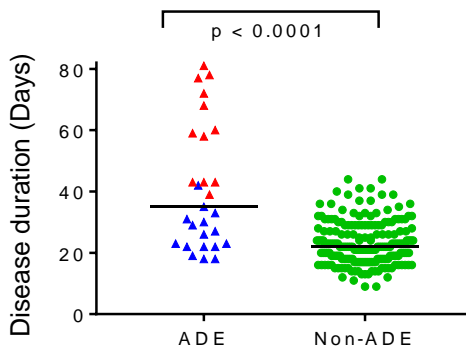
G



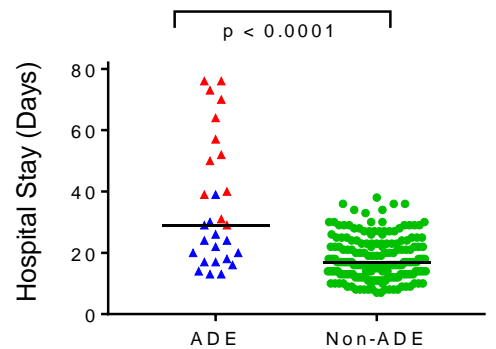
H

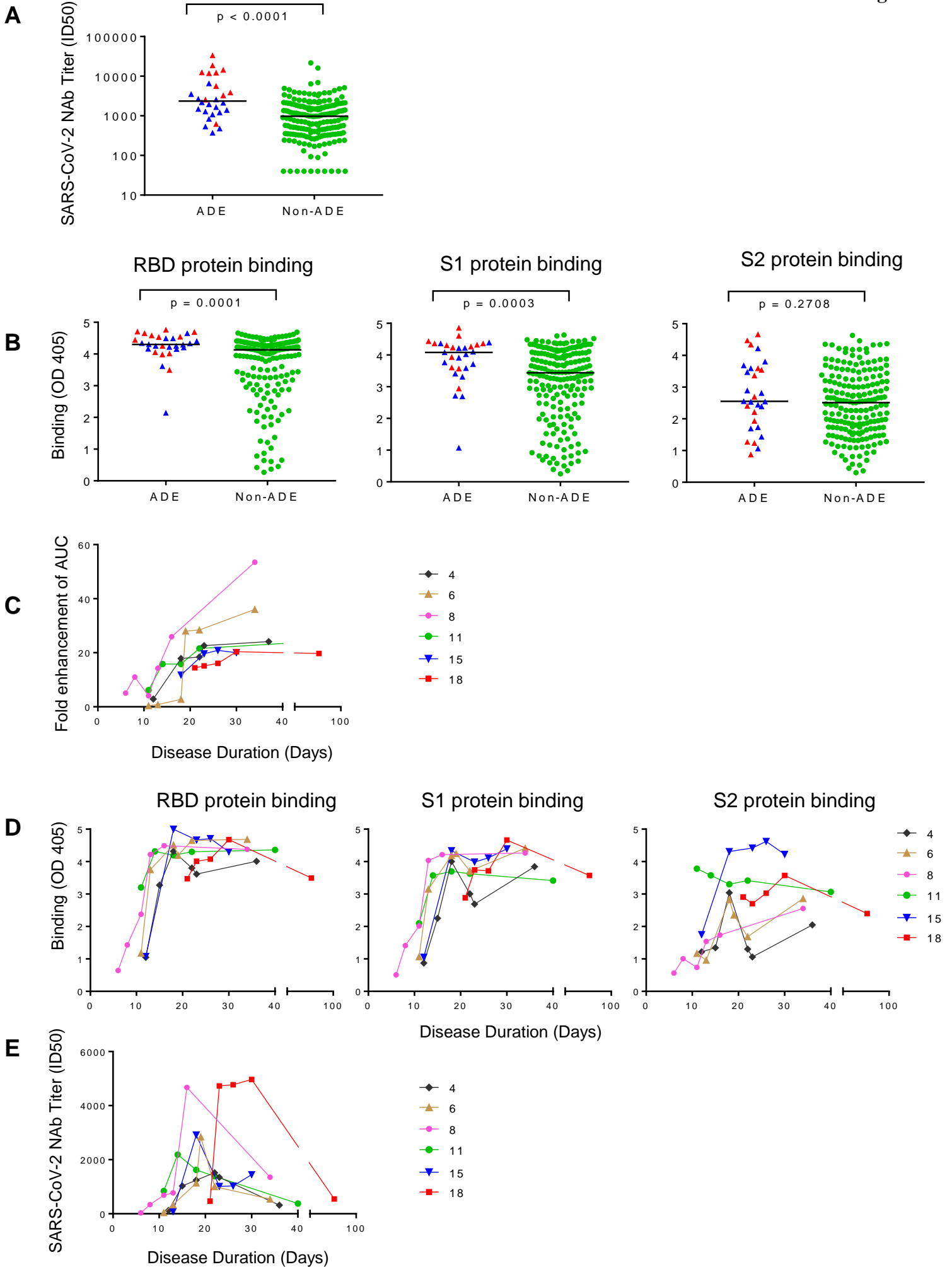


I



J





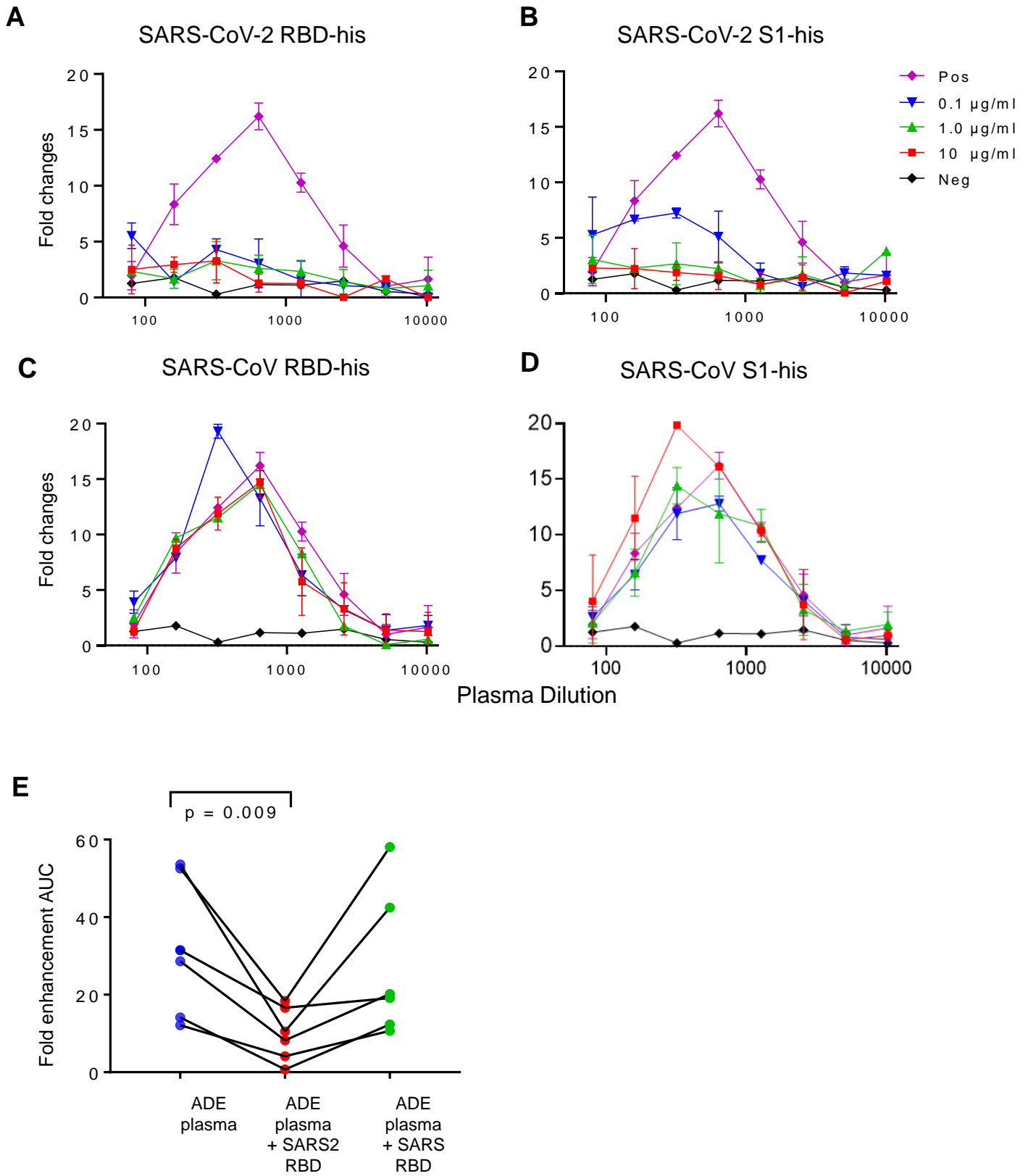
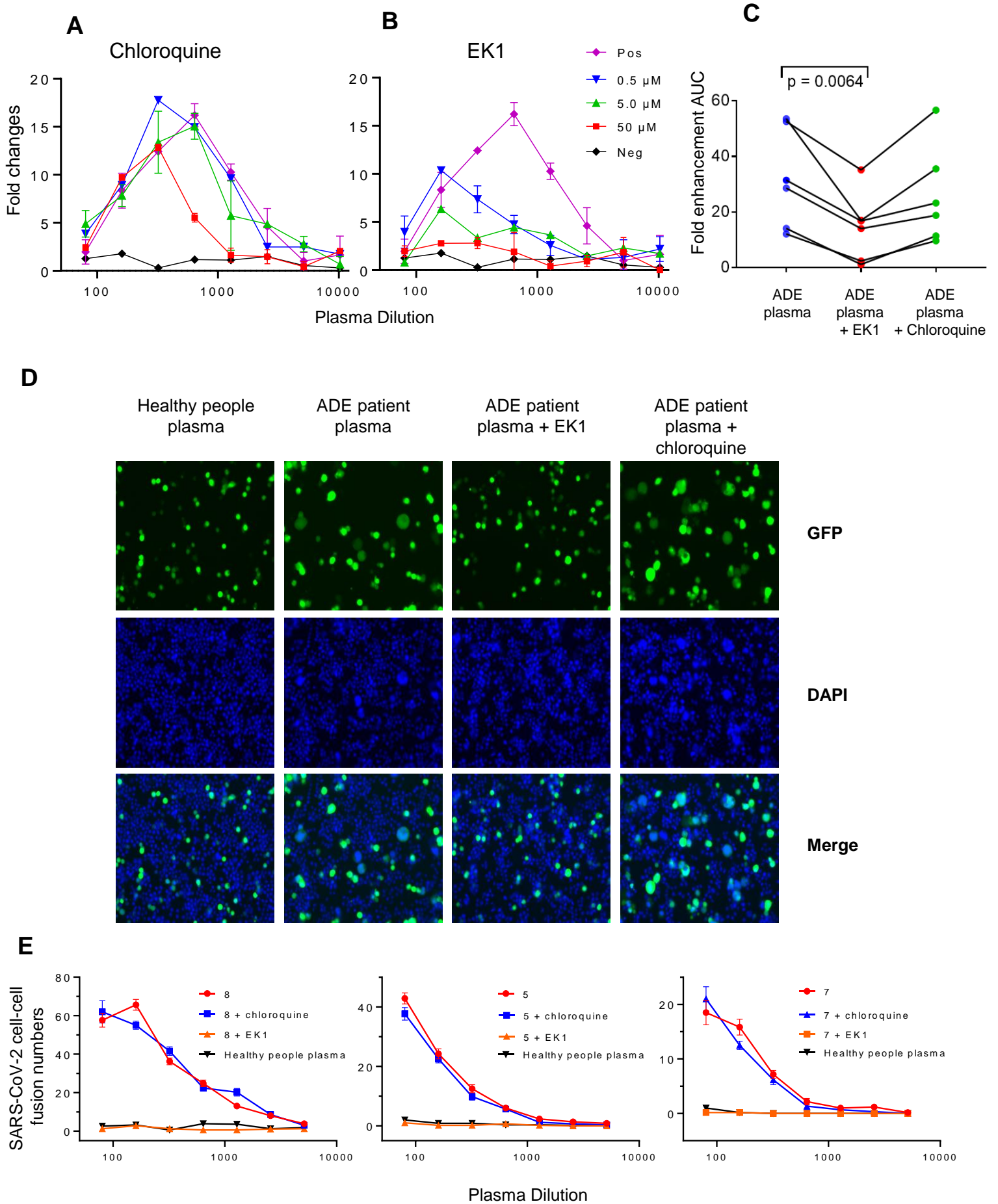
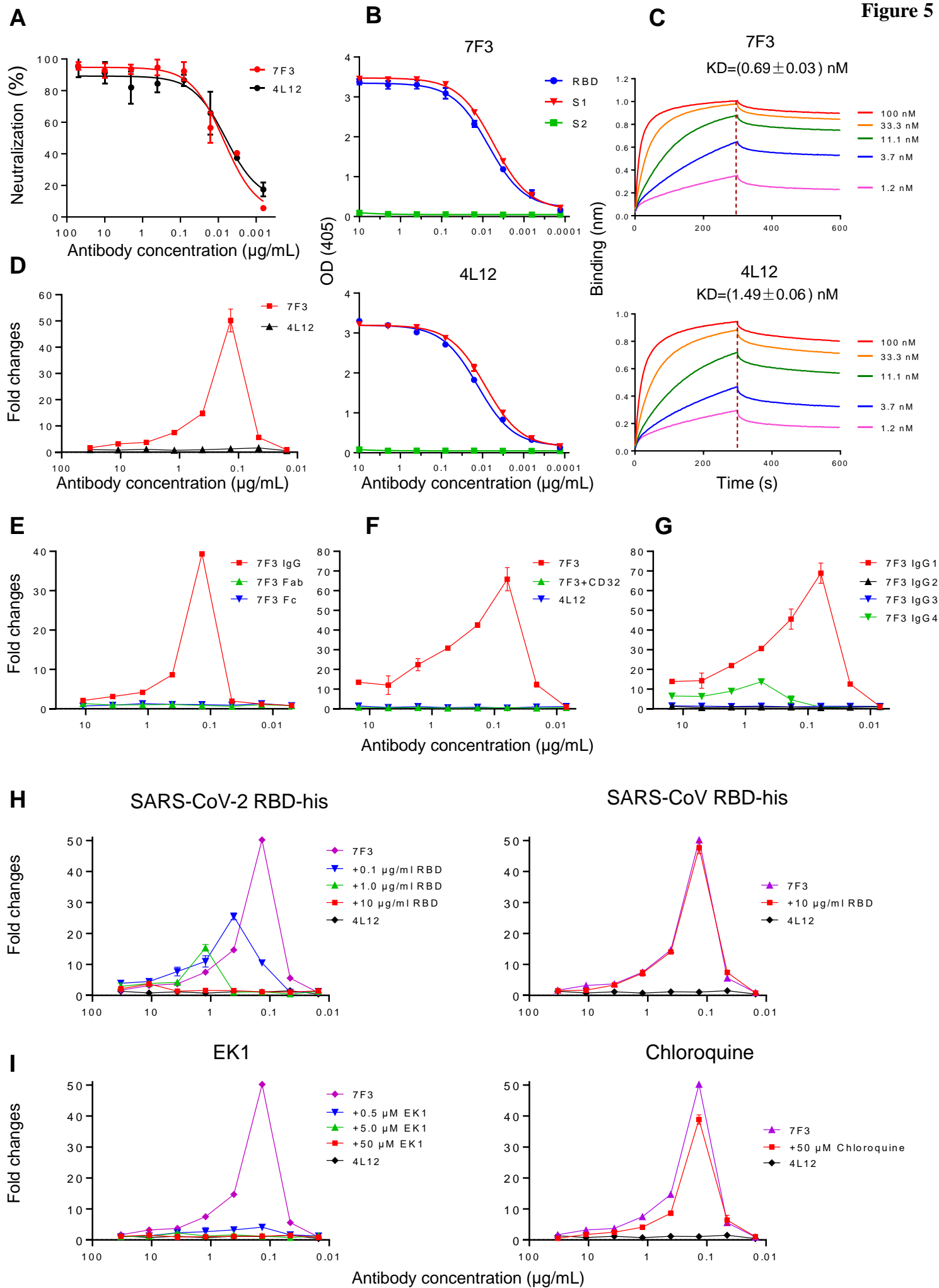
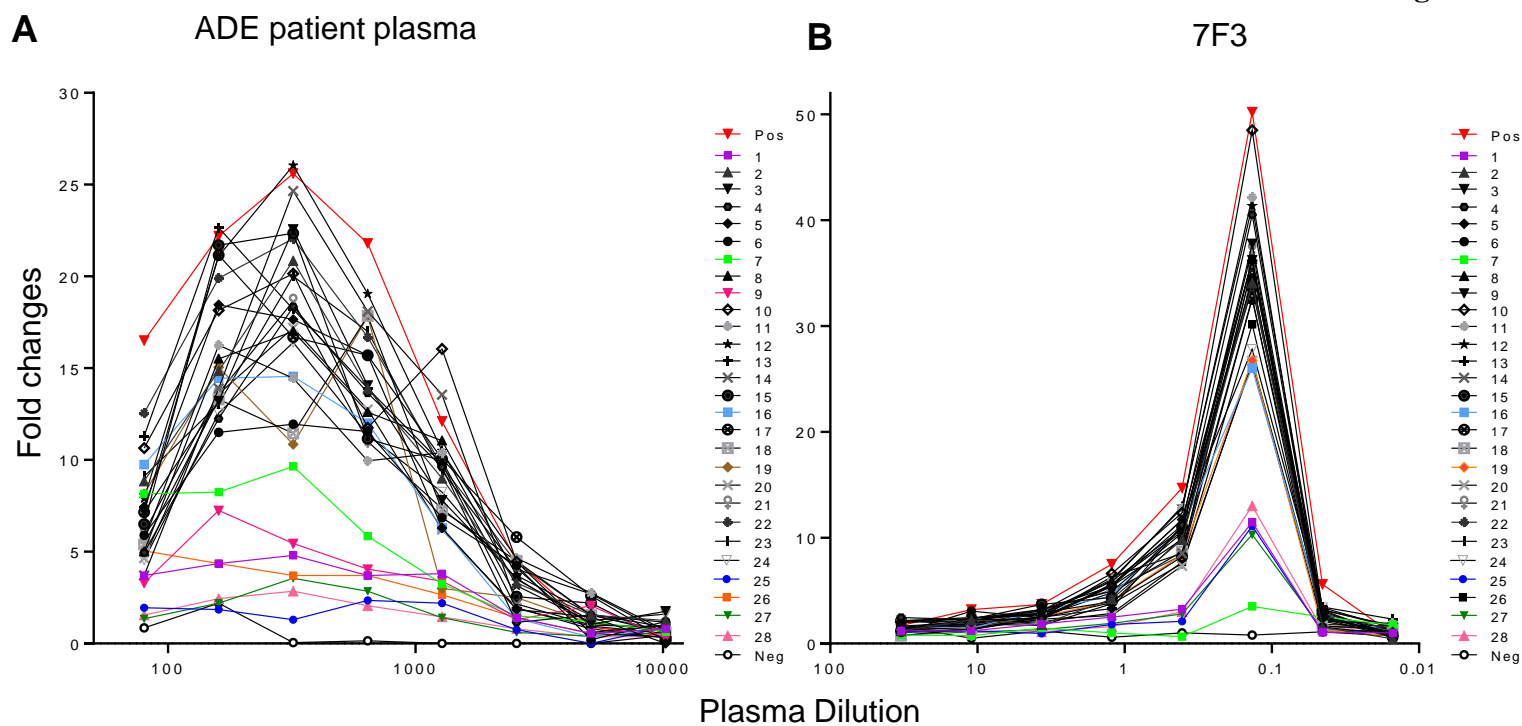


Figure 4





**C**

| Peptide ID | Peptide sequence | S1 region | AUC change (%) | |
|------------|------------------------|-----------|----------------|---------|
| | | | Plasma | 7F3 mAb |
| 1 | KSFTVEKGIY QTSNFRVQPT | 304-323 | 85 | 82 |
| 2 | QTSNFRVQPT ESIVRFPNIT | 314-333 | 24 | 42 |
| 3 | ESIVRFPNIT NLCPFGEVFN | 324-343 | 27 | 33 |
| 4 | NLCPFGEVFN ATRFASVYAW | 334-353 | 37 | 27 |
| 5 | ATRFASVYAW NRKRISNCVA | 344-363 | 42 | 33 |
| 6 | NRKRISNCVA DYSVLNSAS | 354-373 | 45 | 40 |
| 7 | DYSVLNSAS FSTFKCYGVS | 364-383 | 74 | 90 |
| 8 | FSTFKCYGVS PTKLNDLCFT | 374-393 | 22 | 33 |
| 9 | PTKLNDLCFT NVYADSFVIR | 384-403 | 75 | 31 |
| 10 | NVYADSFVIR GDEVQRQIAPG | 394-413 | 10 | 12 |
| 11 | GDEVQRQIAPG QTGKIADYNY | 404-423 | 13 | 23 |
| 12 | QTGKIADYNY KLPDDFTGCV | 414-433 | 15 | 21 |
| 13 | KLPDDFTGCV IAWNSNNLDS | 424-443 | 36 | 32 |
| 14 | IAWNSNNLDS KVGGNYNLY | 434-453 | 18 | 37 |
| 15 | KVGGNYNLY RLFKSNLKP | 444-463 | 24 | 36 |
| 16 | RLFKSNLKP FERDISTEY | 454-473 | 61 | 52 |
| 17 | FERDISTEY QAGSTPCNGV | 464-483 | 0 | 42 |
| 18 | QAGSTPCNGV EGFNCYFPLQ | 474-493 | 27 | 43 |
| 19 | EGFNCYFPLQ SYGFQPTNGV | 484-503 | 63 | 52 |
| 20 | SYGFQPTNGV GYQPYRVVVL | 494-513 | 43 | 46 |
| 21 | GYQPYRVVVL SFELLHAPAT | 504-523 | 39 | 34 |
| 22 | SFELLHAPAT VCGPKKSTNL | 514-533 | 13 | 35 |
| 23 | VCGPKKSTNL VKNKCVNFN | 524-543 | 52 | 49 |
| 24 | VKNKCVNFN NGLTGTGVL | 534-553 | 33 | 43 |
| 25 | NGLTGTGVL ESNKKFLPFQ | 544-563 | 95 | 83 |
| 26 | ESNKKFLPFQ QFGRDIADTT | 554-573 | 88 | 46 |
| 27 | QFGRDIADTT DAVRDPQTLE | 564-583 | 95 | 82 |
| 28 | DAVRDPQTLE ILDITPCSFG | 574-593 | 96 | 79 |

A

| Mutants \ mAb | IC50 ($\mu\text{g/ml}$) | | Fold change relative to WT | |
|---------------------------------------|---------------------------|---------|----------------------------|-------|
| | 7F3 | 4L12 | 7F3 | 4L12 |
| SARS2 WT | 0.00684 | 0.00452 | 1 | 1 |
| V341I | 0.01569 | 0.03091 | 2 | 7 |
| F342L | >50 | >50 | 7309 | 11072 |
| V367F | 0.00771 | 0.00585 | 1 | 1 |
| F374A | 0.01368 | 0.00862 | 2 | 2 |
| R408I | 0.00675 | 0.00373 | 1 | 1 |
| D427A | 0.03808 | 0.01445 | 6 | 3 |
| A435S | 0.00318 | 0.00434 | 0.5 | 1 |
| N439K | 0.02427 | 0.01533 | 4 | 3 |
| N450G | 0.00503 | 0.00612 | 1 | 1 |
| L452R | 0.00571 | 0.01573 | 1 | 3 |
| P463A | 0.01800 | 0.02760 | 3 | 6 |
| I472V | 0.00020 | 0.01140 | 0 | 3 |
| A475V | 0.00878 | 0.01915 | 1 | 4 |
| G476S | 0.01044 | 0.01828 | 2 | 4 |
| S477A | 0.02524 | 0.00703 | 4 | 2 |
| V483A | 0.00467 | 0.00723 | 1 | 2 |
| F490L | 0.00530 | 0.00843 | 1 | 2 |
| P491A | >50 | >50 | 7309 | 11072 |
| G504N | 0.00824 | 0.00421 | 1.2 | 1 |
| Y508H | 0.00262 | 0.01541 | 0.4 | 3 |
| E516A | >50 | >50 | 7309 | 11072 |
| L517A | 0.00896 | 0.00841 | 1 | 2 |
| D614G | 0.00609 | 0.01293 | 1 | 3 |
| A831V | 0.00559 | 0.00945 | 1 | 2 |
| No. of mutants | 25 | 25 | | |
| IC ₅₀ <50 $\mu\text{g/ml}$ | 88% | 88% | | |
| IC ₅₀ <1 $\mu\text{g/ml}$ | 88% | 88% | | |
| GM IC ₅₀ * | 0.007 | 0.010 | | |
| Median IC ₅₀ | 0.007 | 0.009 | | |

* Geometric Mean IC₅₀ concentration is $\mu\text{g/ml}$.

B

| RBD protein mutants | % of Binding relative to WT | |
|---------------------|-----------------------------|------|
| | 7F3 | 4L12 |
| WT RBD-Fc | 1.00 | 1.00 |
| Q321L | 1.00 | 1.00 |
| T323A | 1.00 | 1.00 |
| F342L | 0.91 | 0.93 |
| V367F | 1.00 | 1.00 |
| V367A | 1.00 | 1.00 |
| A372T | 1.03 | 1.04 |
| F374A | 1.02 | 0.84 |
| S375A | 1.03 | 0.97 |
| T376A | 1.02 | 0.90 |
| F377A | 1.03 | 0.92 |
| S383A | 1.06 | 0.96 |
| P384A | 1.05 | 0.89 |
| T385A | 1.00 | 0.87 |
| K386A | 0.99 | 0.84 |
| F392A | 1.00 | 0.88 |
| Q414E | 0.99 | 1.00 |
| D427A | 0.90 | 0.63 |
| D428A | 1.04 | 0.91 |
| A435G | 0.92 | 0.94 |
| N439K | 1.00 | 0.98 |
| G446V | 0.98 | 0.97 |
| N451G | 1.00 | 1.01 |
| L452R | 1.00 | 0.99 |
| K458N | 0.99 | 1.00 |
| I472V | 0.98 | 1.02 |
| A475V | 0.99 | 0.96 |
| T478I | 1.00 | 1.02 |
| V483A | 0.99 | 0.99 |
| V483I | 1.00 | 1.00 |
| F490L | 0.98 | 0.96 |
| P491A | 0.06 | 0.06 |
| G504N | 1.00 | 0.99 |
| Y508H | 0.99 | 1.00 |
| E516A | 1.02 | 0.85 |
| L517A | 1.00 | 0.83 |
| H519P | 1.01 | 1.00 |
| QT414-415AA | 1.01 | 0.94 |
| NNL439-441AAA | 1.01 | 0.90 |
| NYN448-450AAA | 0.92 | 0.71 |
| GST476-478AAA | 0.95 | 0.65 |
| NGV481-483AAA | 0.91 | 0.65 |
| NGV500-502AAA | 1.00 | 0.99 |
| YQP504-506AAA | 0.96 | 0.48 |

C

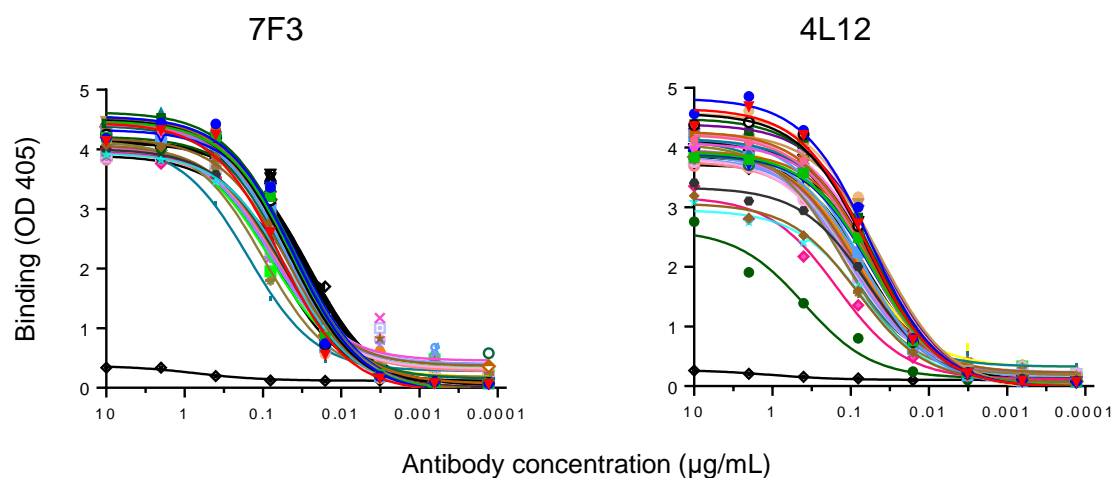
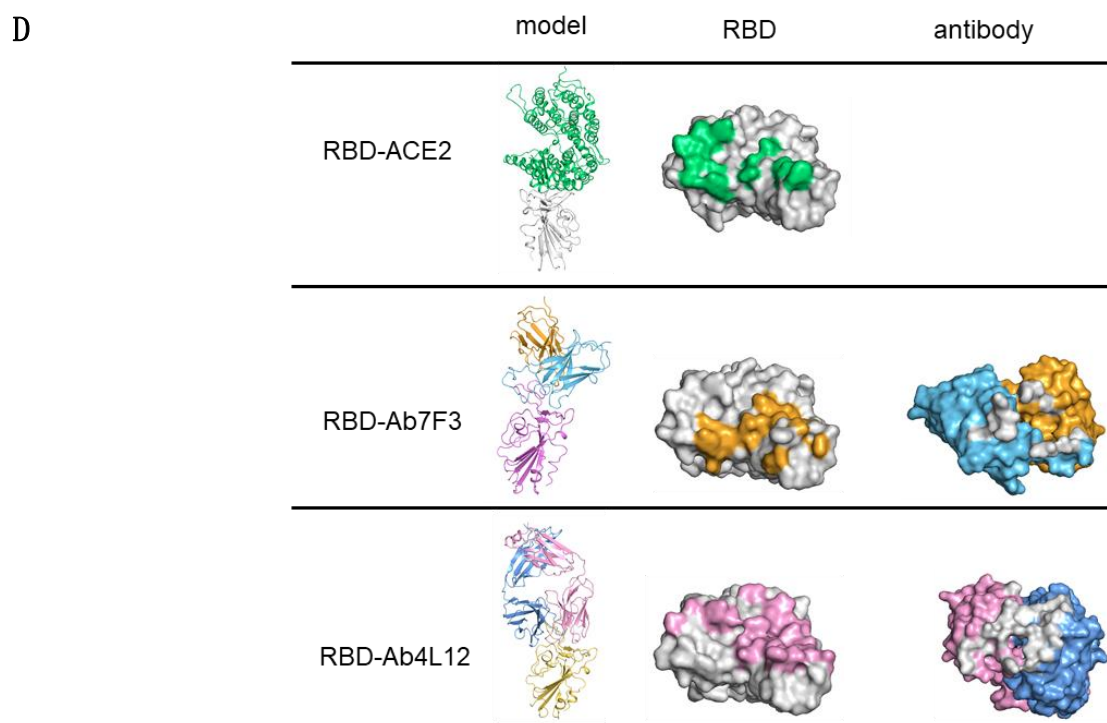
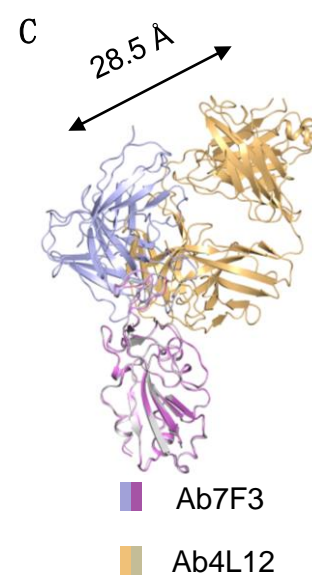
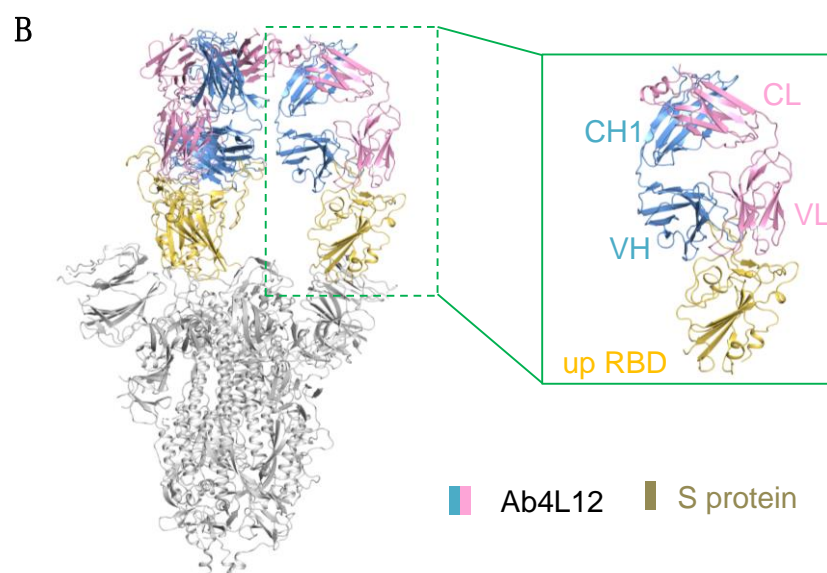
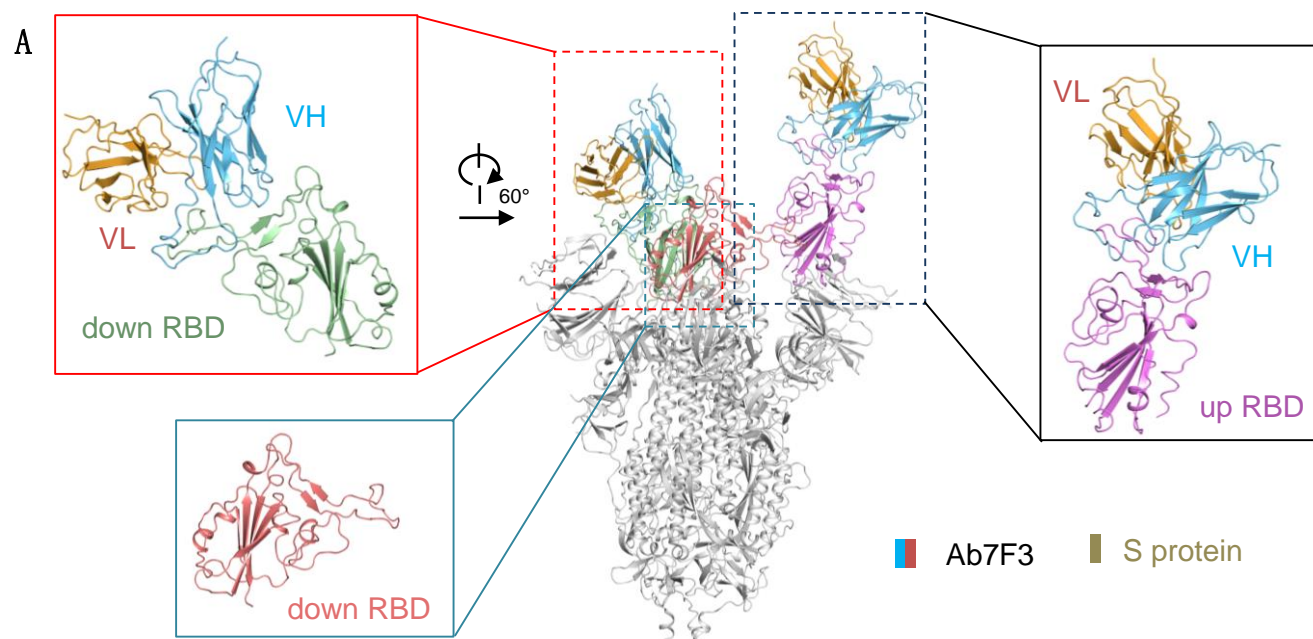
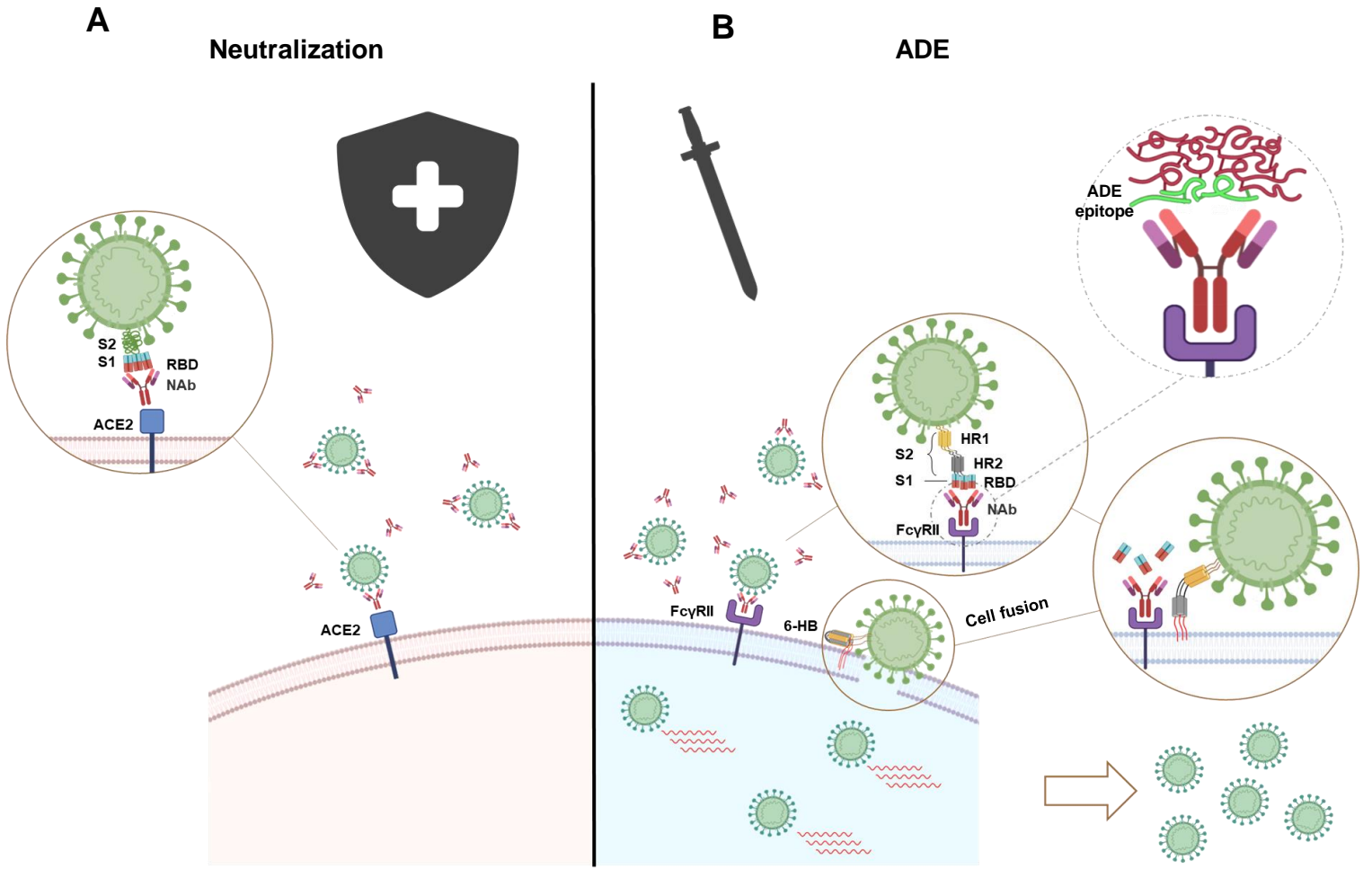


Figure 8





1

Supplementary Table and Figures

2

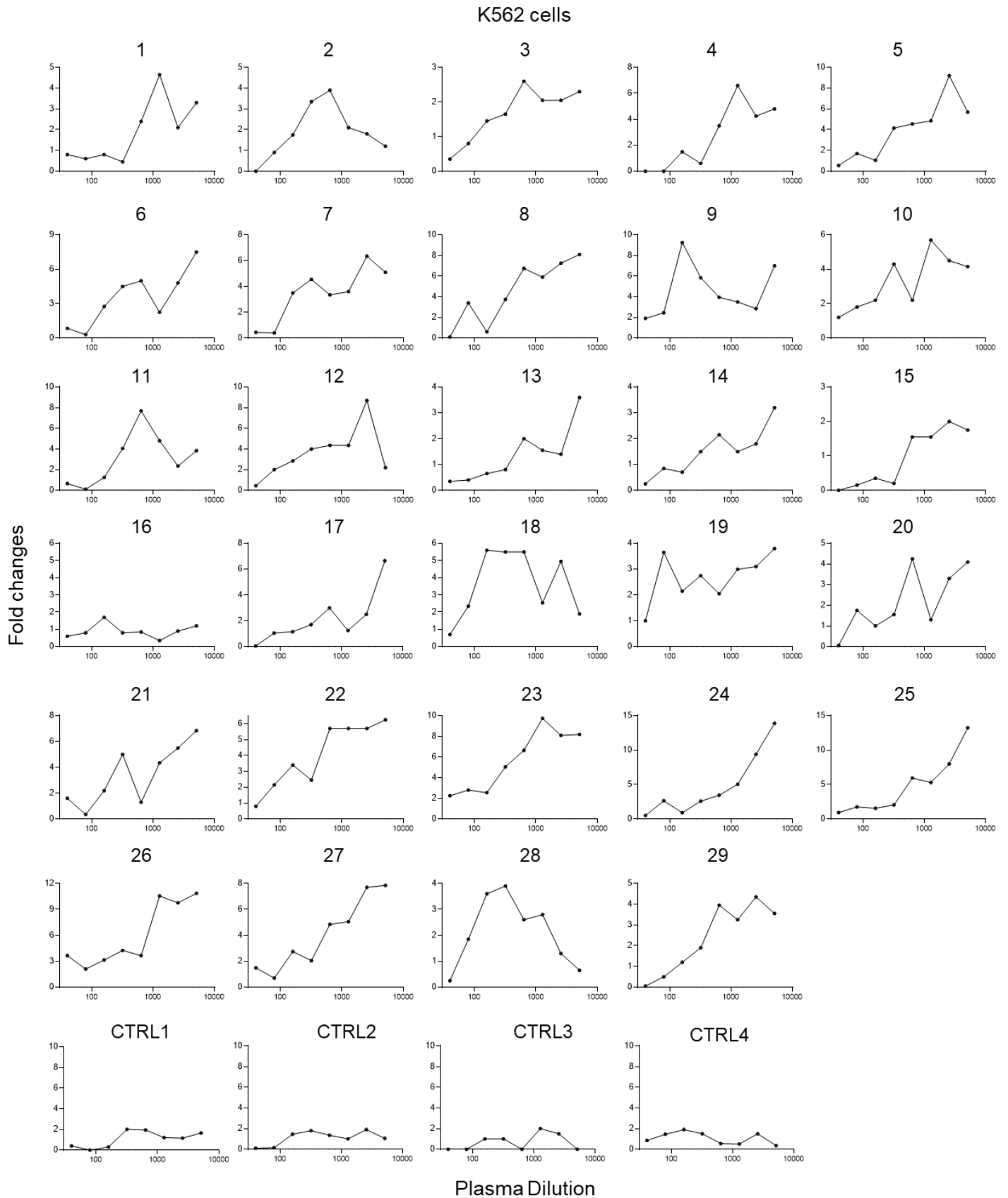
Table S1. Cryo-EM data collection and refinement statistics.

| Data collection | | | | |
|---|--|------------|--------------|------------|
| EM equipment | Titan Krios (Thermo Fisher Scientific) | | | |
| Voltage (kV) | 300 | | | |
| Detector | Gatan K3 Summit | | | |
| Energy filter | Gatan GIF Quantum, 20 eV slit | | | |
| Pixel size (Å) | 1.087 | | | |
| Electron dose (e-/Å ²) | 50 | | | |
| Defocus range (µm) | -1.2 ~ -2.2 | | | |
| Sample | S-ECD+Ab7F3 | | S-ECD+Ab4L12 | |
| Number of collected micrographs | 1,877 | | 1,219 | |
| Number of selected micrographs | 1,840 | | 1,199 | |
| 3D Reconstruction | | | | |
| Software | Relion 3.0 | | | |
| Sample | Overall | subcomplex | Overall | subcomplex |
| Number of used particles (Overall) | 91,303 | 29,903 | 314,098 | 557,717 |
| Resolution (Å) | 3.3 | 6.3 | 3.0 | 3.5 |
| Symmetry | C1 | | | |
| Map sharpening B-factor (Å ²) | -90 | | | |
| Refinement | | | | |
| Software | Phenix | | | |
| Cell dimensions | | | | |
| a=b=c (Å) | 313.056 | | | |
| α=β=γ (°) | 90 | | | |
| Model composition | | | | |
| Protein residues | 3,508 | | 4,308 | |
| Side chains assigned | 3,458 | | 4,308 | |
| Sugar | 71 | | 71 | |
| RMS deviations | | | | |
| Bond lengths (Å) | 0.009 | | 0.007 | |
| Bond Angles (°) | 0.795 | | 0.720 | |
| Ramachandran plot statistics (%) | | | | |
| Preferred | 88.80 | | 91.26 | |
| Allowed | 10.90 | | 8.60 | |
| Outlier | 0.30 | | 0.13 | |

3

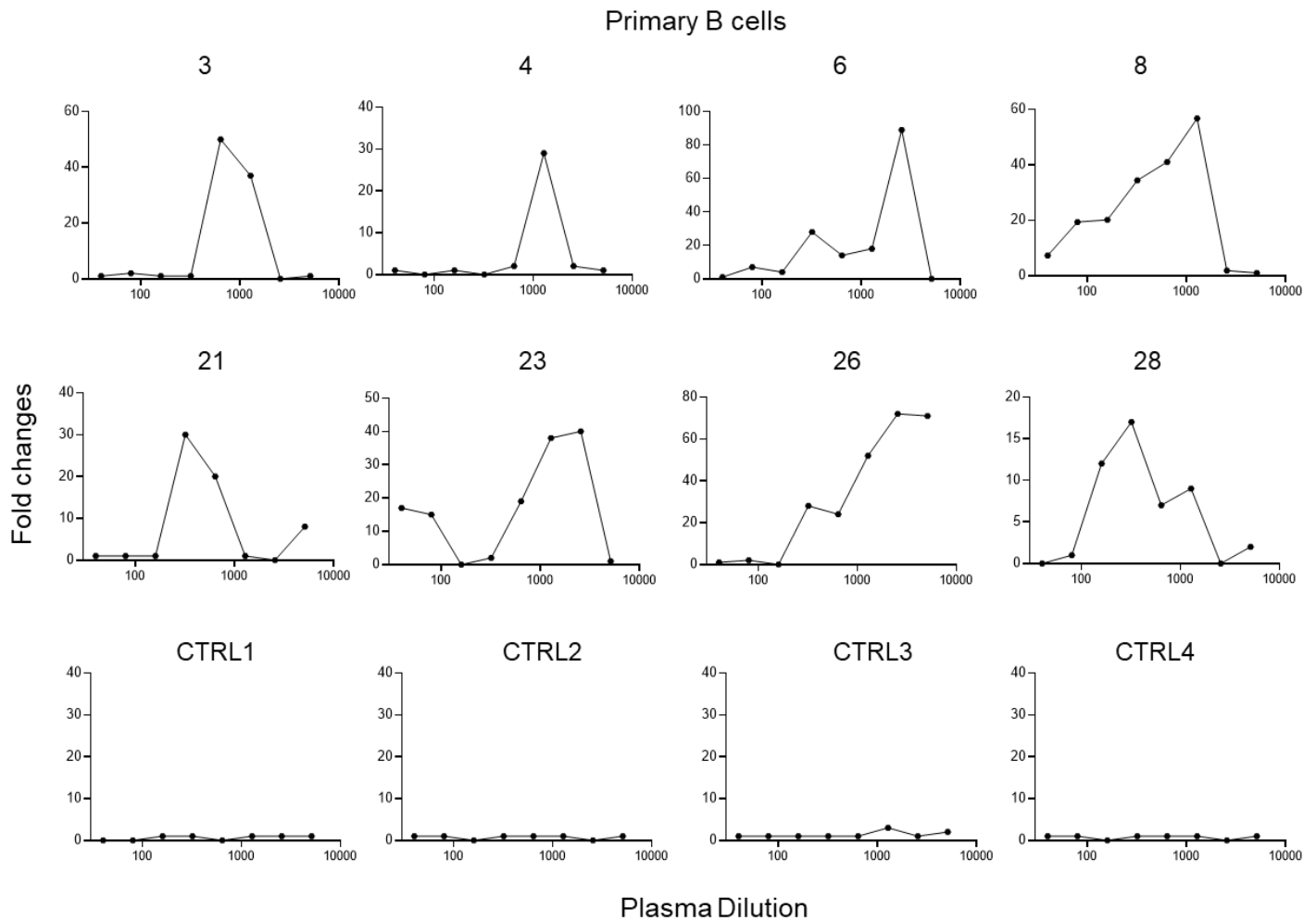
5 **Figure S1. Enhancement of SARS-CoV-2 infection of Raji cells by patient plasma.**

6 (A) 29 plasma from patients recovered from mild (1-16) and severe COVID-19 (17-
7 29) showed enhancement of SARS-CoV-2 infection of Raji cells. Ten plasma from
8 uninfected donors were used as controls. Plasma samples were two-fold serially diluted
9 and tested for ADE of SARS-CoV-2 infection of Raji cells. The assay was performed
10 in duplicate wells and mean fold changes of luciferase reading comparing to virus
11 control are shown.



12 **Figure S2. Enhancement of SARS-CoV-2 infection of K562 cells by COVID-19**
13 **patient plasma.**

14 29 plasma from patients who recovered from mild (1-16) and severe COVID-19 (17-
15 29) showed enhancement of SARS-CoV-2 infection of K562 cells. Four plasma from
16 uninfected donors were used as controls. The assay was performed in duplicate wells
17 and mean fold changes of luciferase reading comparing to virus control are shown.



18

19 **Figure S3. Enhancement of SARS-CoV-2 infection of primary B cells by COVID-**
20 **19 patient plasma.**

21 Eight representative plasma from patients with mild COVID-19 (3, 4, 6, and 8) and
22 severe COVID-19 (21, 23, 26, and 28) showed enhancement of SARS-CoV-2 infection
23 of primary B cells. Four plasma from uninfected donors were used as controls.

24

25

26

27

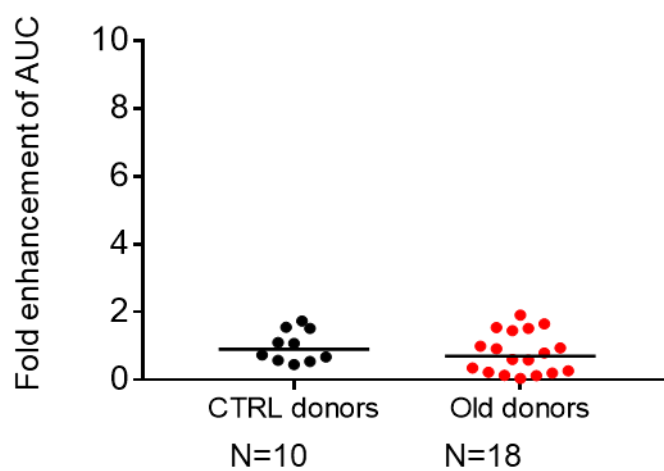
28

29

30

31

32

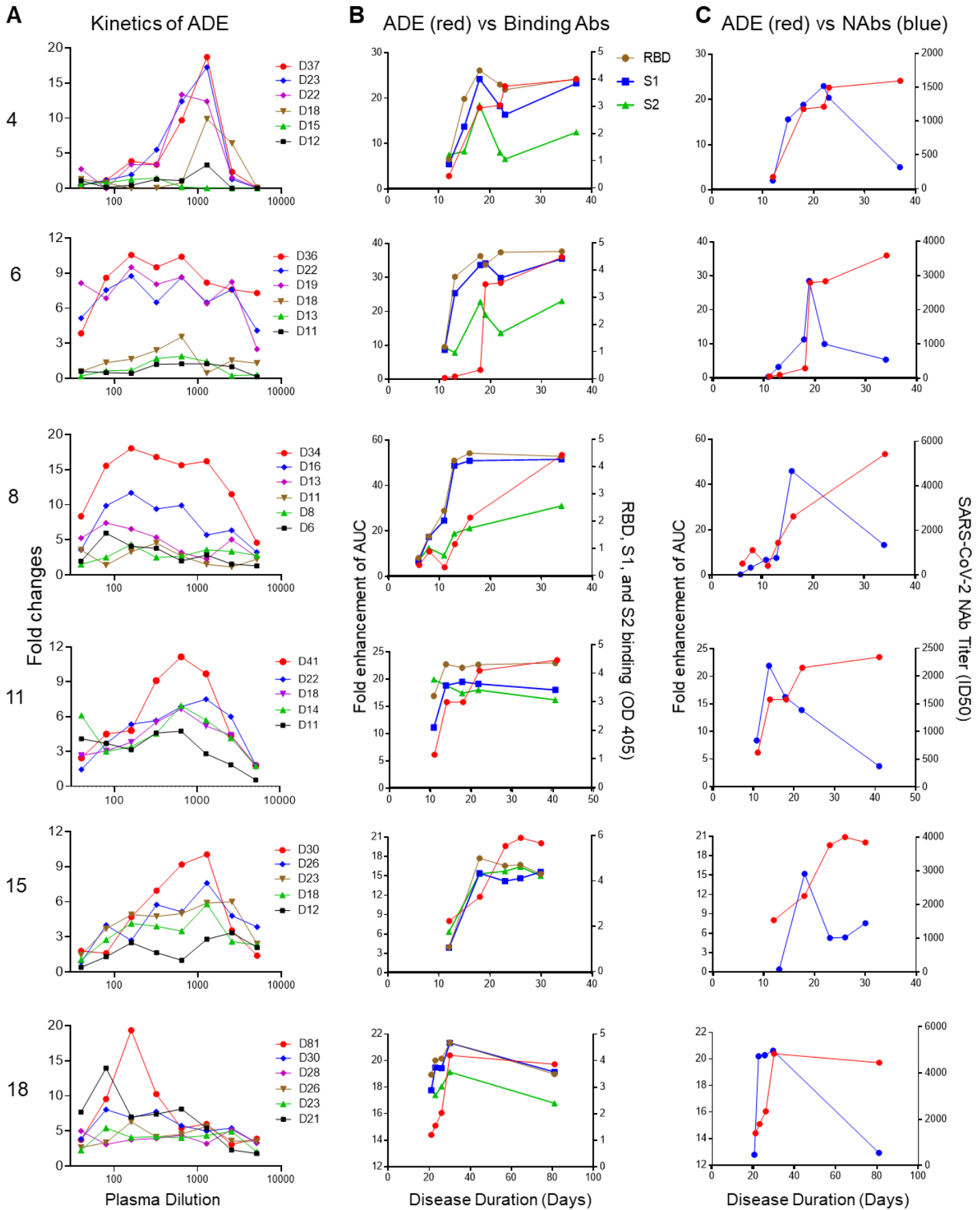


33

34

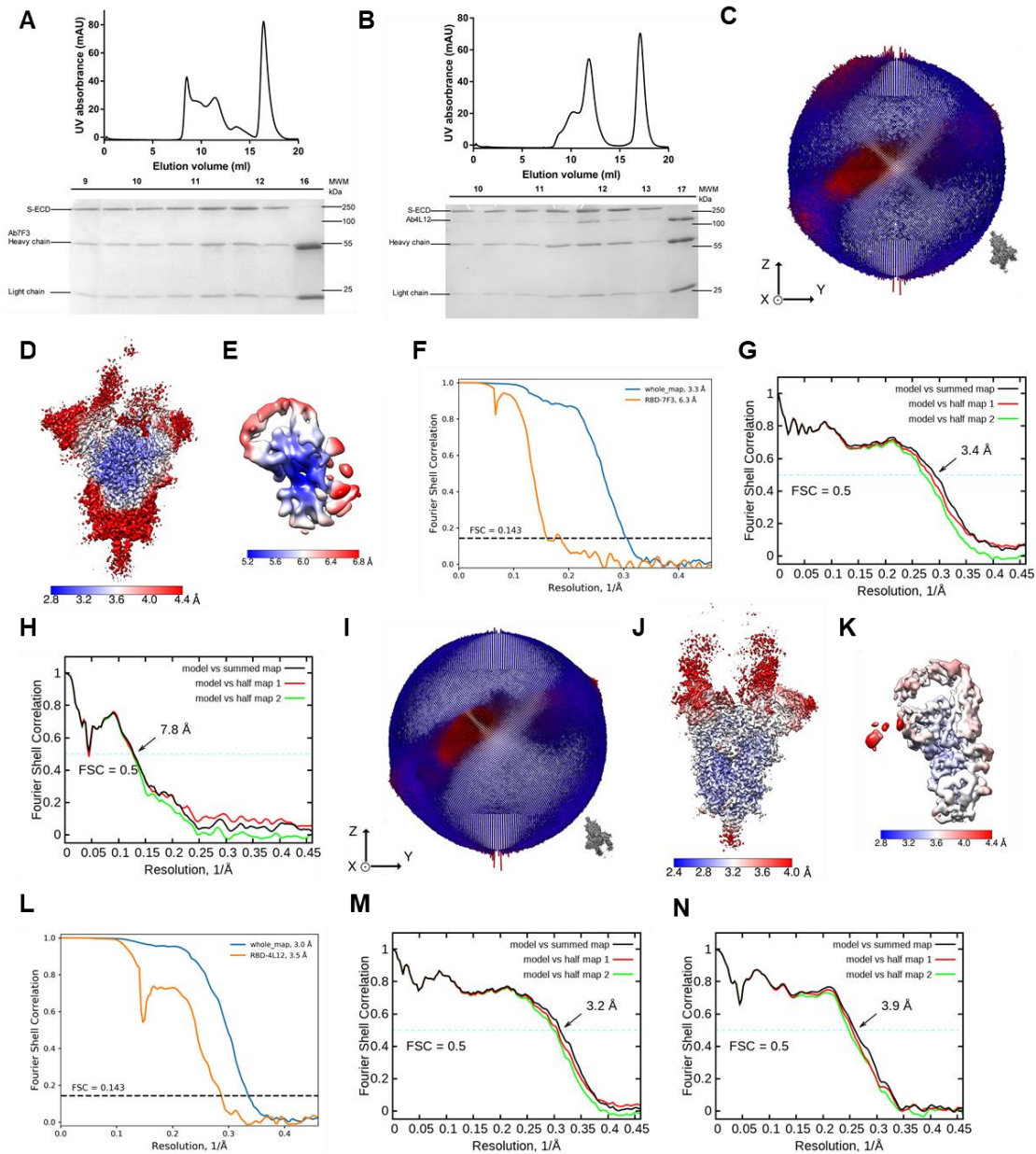
35 **Figure S4.** Comparison of ADE effect in plasma from uninfected control donors and

36 uninfected older donors.



38 **Figure S5. Kinetics of SARS-CoV-2 ADE, spike-binding antibodies and NAbs**

39 (A) Kinetics of SARS-CoV-2 ADE effect of six ADE patients are shown. Kinetics of
40 spike-binding antibodies (right Y axis), targeting RBD (brown), S1 (green), and S2
41 (blue) (B) and kinetics of NAbs (right Y axis, blue) (C) in six COVID-19 patient plasma
42 are shown and compared with the kinetics of ADE effect (left Y axis, red) in the same
43 patient. 1:400 diluted plasma was incubate with RBD, S1, or S2 protein.



44

45

46 **Figure S6. Cryo-EM analysis of S-ECD of SARS-CoV-2 bound with 4A8 complex.**

47 (A)-(B) Representative SEC purification profile of the S-ECD of SARS-CoV-2 in

48 complex with Ab7F3 and Ab4L12, respectively. (C) Euler angle distribution in the final

49 3D reconstruction of S-ECD of SARS-CoV-2 bound with Ab7F3 complex. (D) and (E)

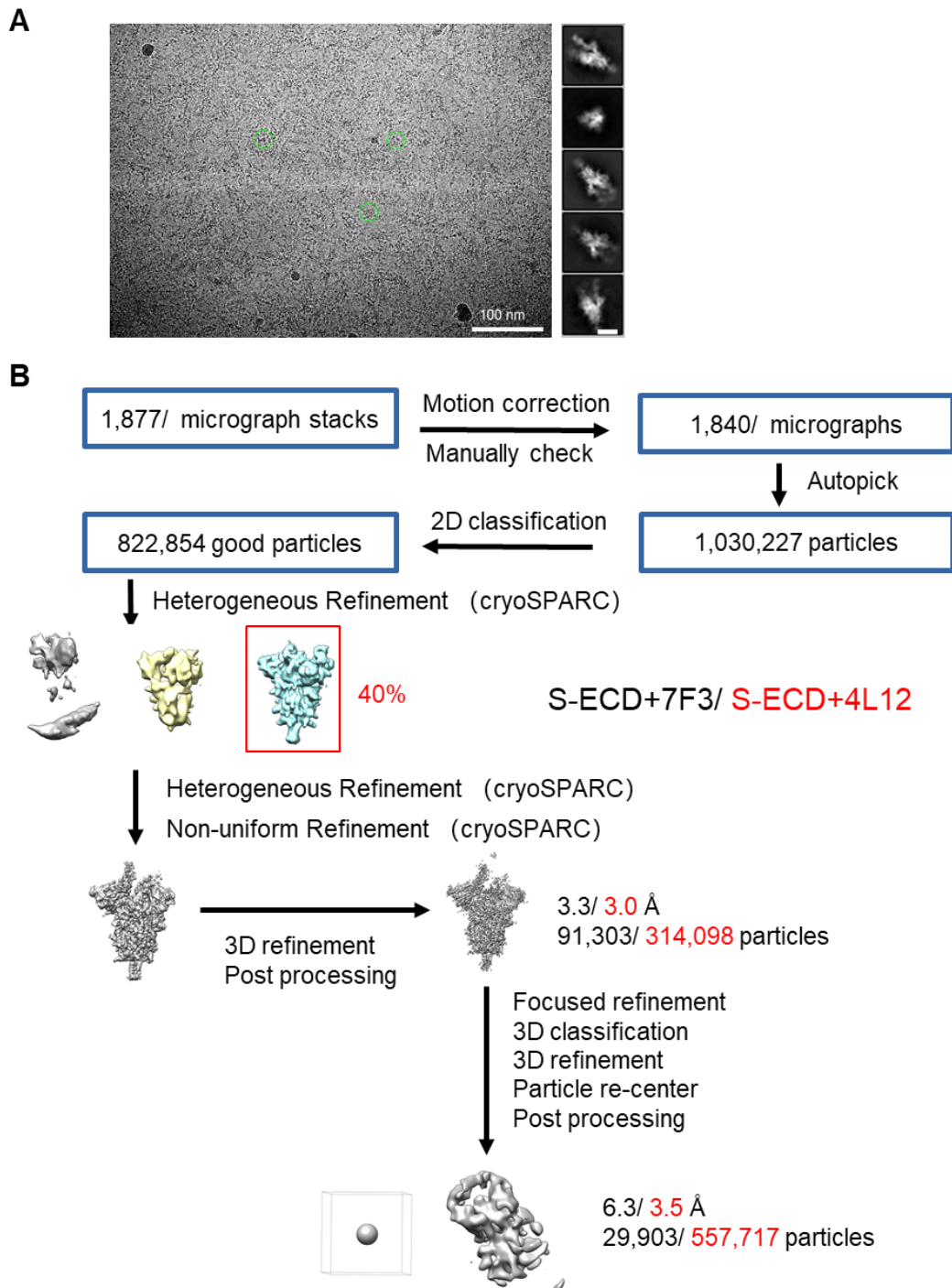
50 Local resolution maps for the 3D reconstruction of the overall structure and RBD-

51 Ab7F3 subcomplex, respectively. (F) FSC curve of the overall structure (blue) and

52 RBD-Ab7F3 subcomplex (orange). (G) FSC curve of the refined model of S-ECD of

53 SARS-CoV-2 bound with Ab7F3 complex versus the overall structure against which it

54 is refined (black); of the model refined against the first half-map versus the same map
55 (red); and of the model refined against the first half-map versus the second half-map
56 (green). The small difference between the red and green curves indicates that the
57 refinement of the atomic coordinates lacks sufficient overfitting. **(H)** FSC curve of the
58 refined model of RBD-Ab7F3 subcomplex, which is the same as **(G)**. **(I)-(N)** is the
59 same as **(C)-(H)**, except for SARS-CoV-2 bound with Ab4L12 complex.
60



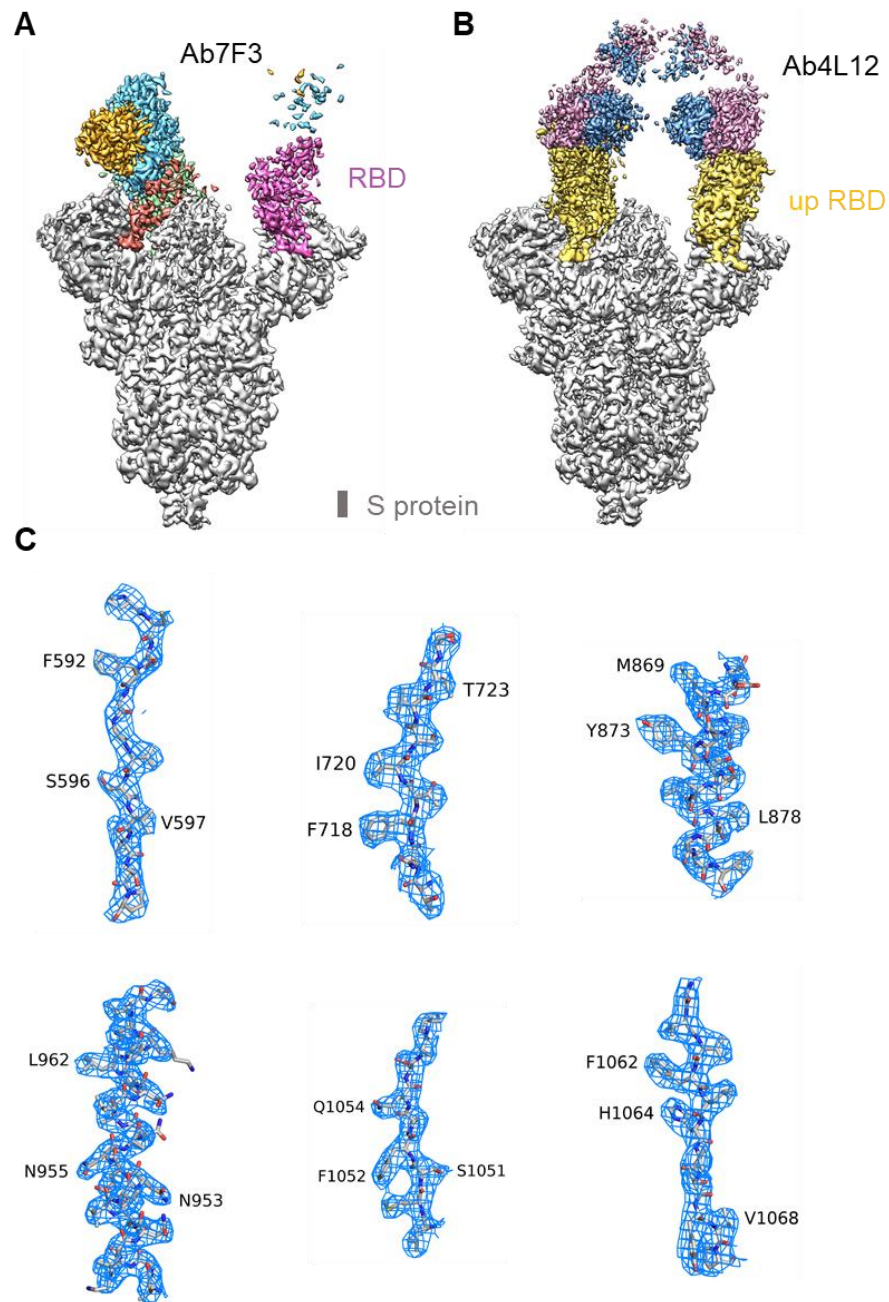
61

62 **Figure S7. Representative cryo-EM image and flowchart for cryo-EM data**
63 **processing.**

64 (A) Representative cryo-EM micrograph and 2D class averages of cryo-EM particle

65 images. The scale bar in 2D class averages is 10 nm. (B) Please refer to the ‘Data

66 Processing’ section in Methods for details.

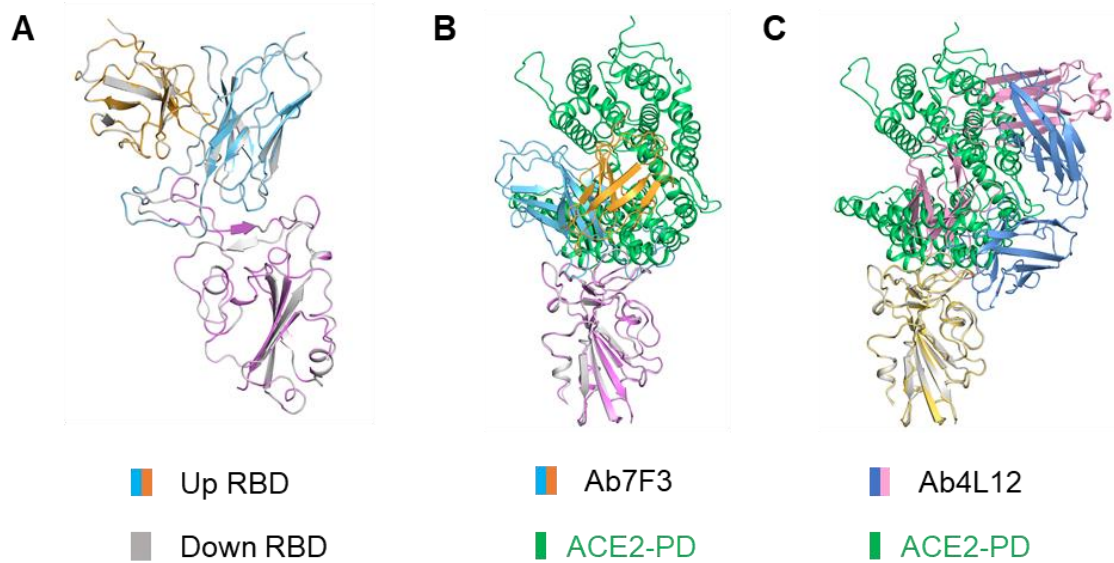


67

68 **Figure S8. Overall maps of S-ECD in complex with mAb and representative**
69 **cryo-EM density maps.**

70 **(A)** The domain-colored cryo-EM maps of S-ECD of SARS-CoV-2 bound with
71 Ab7F3 complex. **(B)** The domain-colored cryo-EM maps of S-ECD of SARS-CoV-2
72 bound with Ab4L12 complex. **(C)** Cryo-EM density map for S-ECD in complex with
73 Ab7F3 is shown at threshold of 6σ .

74



75

76 **Figure S9. Structural alignment between RBD-mAb subcomplex and RBD-PD**
77 **complex (PDB ID: 6M0J).**

78 (A) Superposition in local structure of “up” RBD-Ab7F3 subcomplex and “down”

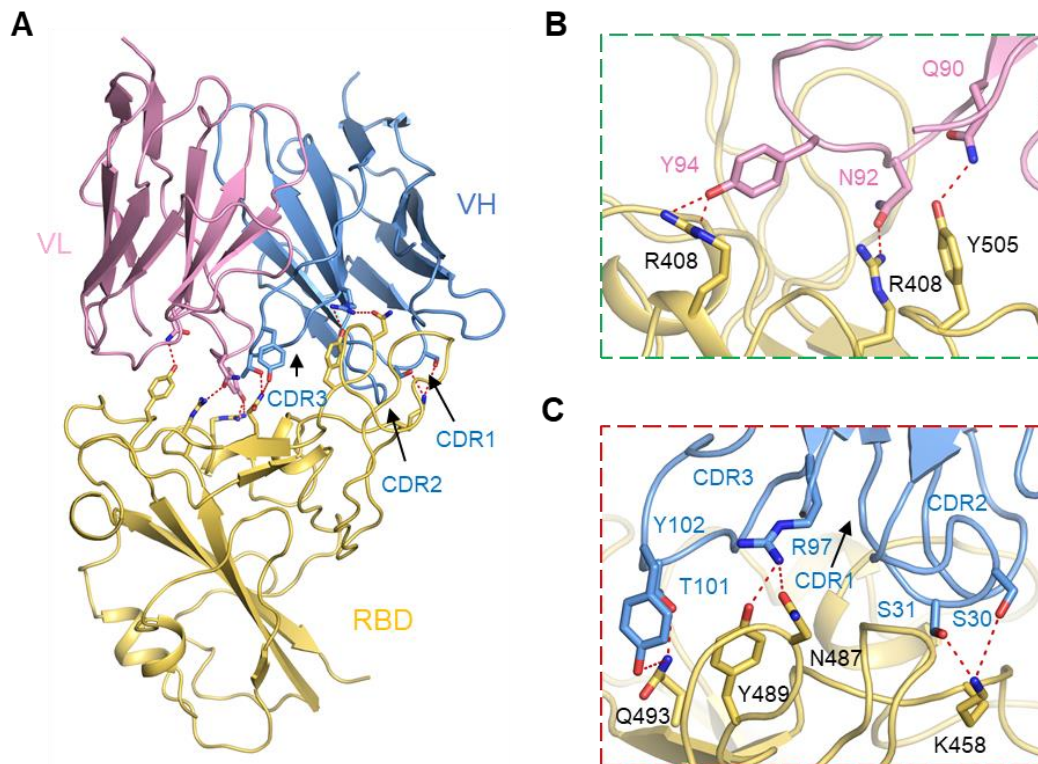
79 RBD-Ab7F3 subcomplex, indicating no difference between the two maps. (B)

80 Structural alignment between RBD-Ab7F3 subcomplex and RBD-PD complex (PDB

81 ID: 6M0J). (C) Structural alignment between RBD-Ab7F3 subcomplex and RBD-PD

82 complex (PDB ID: 6M0J).

83



84

85 **Figure S8. Interactions between the RBD and Ab4L12.**

86 (A) Extensive hydrophilic interactions on the interface between RBD and Ab4L12.

87 (B) and (C) Detailed analysis of the interface between RBD and Ab 4L12. Polar

88 interactions are indicated by red dashed lines.

89